A Precision Measurement of the η Lifetime via the Primakoff Effect

The PrimEx Collaboration

December 15, 2008

Contents

Abstract

We propose to perform a precision measurement of the $\eta \to \gamma\gamma$ decay width in Hall D of Jefferson Lab via the Primakoff effect. This experiment will not only resolve a long standing puzzle of the experimental discrepancy between the Primakoff and collider measurement results, but will also significantly reduce the overall error bar on this important quantity, resulting in a direct improvement on all other partial η decay widths. A precision measurement of the $\eta \to \gamma\gamma$ decay width will have significant impact on the experimental determination of fundamental parameters, such as the ratios of the light quark masses (m_u, m_d, m_s) and the $\eta - \eta^{'}$ mixing angle, and will provide a sensitive test of QCD symmetries in the chiral limit.

1　Introduction

The availability of high quality, high duty factor 12 GeV electron beams at JLab will enable unprecedented new opportunities to perform precise measurements of the electromagnetic properties of pseudoscalar mesons. We have developed a comprehensive experimental program in the last 10 years to study the two photon decay widths, $\Gamma_{\gamma\gamma}$, and the transition form factors, $F_{\gamma\gamma^*}$, of the π^0, η, and η' pseudoscalar mesons. The original proposal was presented to the JLab PAC18 special review in July 2000. It received a high recommendation from the PAC [1] and was identified in the "Executive Summary" of the CEBAF 12 GeV upgrade white paper "Science Driving the 12 GeV CEBAF Upgrade" as one of the major physics programs for the lab's long-range plan. This project was re-confirmed by PAC23 (the second 12 GeV special review) in 2003 and remains a top priority physics program with the PAC recommendation "to be developed as one of the leading scientific projects for the next generation of experiments at Jefferson Lab"[2]. The measurement of the η radiative decay width described below will be the first experiment among a series of other measurements in the Primakoff 12 GeV program.

2　Motivation

In the chiral limit, the condensation of quark-anti-quark pairs in the QCD vacuum spontaneously breaks $SU_L(3) \times SU_R(3)$ symmetry down to the flavor $SU(3)$ symmetry. As a result, there are eight massless Goldstone Bosons corresponding to the eight spontaneously broken symmetry generators. These Goldstone Bosons are identified with the octet of pseudoscalar mesons (π^0, $\pi^{\pm}$, $K^{\pm}$, K^0, $\bar{K}^0$, and η). In reality, the quark masses are non zero (albeit small), thus breaking the chiral symmetry explicitly and giving rise to masses for the Goldstone Bosons following the mechanism discovered by Gell-Mann, Oakes and Renner [3]. As the heaviest member in the octet pseudoscalar meson family, the η plays a special role. It has an interesting feature that all its strong and electromagnetic decays are forbidden in lowest order due to P, PC, C, G-parity symmetries and angular momentum conservation, or suppressed by the anomaly[4]. The width of the η is about 1.29 keV, which is 5 orders of magnitude smaller than a typical strong decay, such as the ρ and ω mesons. This feature makes η decay 10^5 times more sensitive than the ρ and ω decays at a comparable branching ratio for testing symmetries of QCD.

As with the π^o, the two-photon decay of the η is directly associated with the chiral anomaly. This is one of the most profound symmetry issues in QCD, namely, the explicit breaking of a classical symmetry by the quantum fluctuations of the quark fields when they couple to a gauge field. This phenomenon is of a pure quantum mechanical origin and can be calculated exactly at all orders in the chiral limit. In QCD there are several observable phenomena that originate from anomalies. One connected to the couplings of the quarks to the gluons is responsible for the non-zero mass of the η' at the chiral limit. The axial anomaly related to the η two-photon decay involves the corresponding coupling of the quarks to photons[5]. In the chiral and large N_c limits, the two-photon decays of η can be predicted. The important question is then what are the effects of the quarks masses and the corrections

due to the fact that $N_c = 3$.

Indeed, the relatively straightforward situation of the chiral limit becomes much more complex in the case in which the quark masses are non-vanishing. In the real world the current quark masses are estimated to be $m_u \sim m_d/2 \sim 5$ MeV and $m_s \sim 150$ MeV at the renormalization QCD scale of about 1 GeV. These masses make the η massive, while $SU(3)$ and isospin breaking induce mixings among the π^o, η and η' mesons. The mixings are expressed in terms of three mixing angles [6]. Writing the eigenstates in the chiral limit on the left, they are expressed in terms of the physical states by

$$\pi_8^0 = \pi^0 - \epsilon\eta - \epsilon'\eta'$$

$$\eta_8 = \cos\theta \ (\eta + \epsilon\pi^0) + \sin\theta \ (\eta' + \epsilon'\pi^0)$$

$$\eta_0 = -\sin\theta \ (\eta + \epsilon\pi^0) + \cos\theta \ (\eta' + \epsilon'\pi^0)$$

A recent global analysis [6] has been performed that uses the two-photon decay widths of the η and η' as input and includes next to leading order chiral corrections as well as $1/N_c$ corrections. It gives: $\epsilon \sim 0.8°$, $\epsilon' \sim 0.3°$ and $\theta \sim -12°$ for these mixing angles.

In recent years, a framework that implements the chiral and $1/N_c$ corrections was developed [7, 8, 6]. This framework is a faithful representation of low energy QCD, relying only on the validity of the chiral expansion in the strange quark mass and the expansion in $1/N_c$. In particular, this implies the assumption that the η' can still be considered as an approximate Goldstone Boson. The framework predicts that the two-photon decays involve two mixing angles, θ_0 and θ_8, and two decay constants, F_0 and F_8, (two-mixing angle scenario [9]). There is also a new low energy constant t_1 to be taken into account at next to leading order in the chiral expansion. It can be estimated using QCD sum rules ($t_1 = -F_\pi^2/m_\rho^4$). With this, the η and η' decay amplitudes into two photons defined as:

$$A_{\eta\gamma\gamma} = \alpha(\frac{1}{24\pi F_0 F_8} \sec(\theta_0 - \theta_8)(\sqrt{3}F_0 \cos\theta_0 - 2\sqrt{6}F_8 \sin\theta_8)$$

$$-\frac{\pi}{18\sqrt{3}F_\pi}t_1((4M_K^2 - 7M_\pi^2)\cos\theta + 2\sqrt{2}(M_K^2 + 2M_\pi^2)\sin\theta))$$

$$A_{\eta'\gamma\gamma} = \alpha(\frac{1}{8\sqrt{3}\pi F_0 F_8} \sec(\theta_0 - \theta_8)(2\sqrt{2}F_8 \cos\theta_8 + F_0 \sin\theta_0)$$

$$+\frac{\pi}{18\sqrt{3}F_\pi}t_1(2\sqrt{2}(M_K^2 + 2M_\pi^2)\cos\theta + (-4M_K^2 + 7M_\pi^2)\sin\theta)) \tag{1}$$

Here θ is the state mixing angle defined earlier.

The fact that there is a well defined theoretical framework makes the η a very important state to be studied with precision as a means to further understand fundamental aspects of QCD. While the width of the $\pi^o \to \gamma\gamma$ will provide the most precise test of the chiral anomaly prediction at leading order, the $\eta \to \gamma\gamma$ decay will be the most sensitive probe for the higher order corrections due to its larger mass. In particular, a precise measurement of $\Gamma(\eta \to \gamma\gamma)$ is crucial to extract the η and η' mixing angle and their decay constants as discussed above.

One important question to ask is: What would be the impact of a more precise measurement of the η two-photon partial width? Right away, it would imply a corresponding improvement in the determination of all other partial widths of the η, as these are determined using the two-photon widths and the corresponding branching ratios. This would therefore have wide ranging implications. One decay that is particularly important is the $\eta \to \pi\pi\pi$ decay (two different final states), which is driven by isospin breaking, and thus gives access to the quark mass ratio $(m_u - m_d)/m_s$. In a very elegant analysis, Leutwyler [10] constructed a relation, now called Leutwyler's ellipse, given by:

$$\left(\frac{m_u}{m_d}\right)^2 + \frac{1}{\mathcal{Q}^2}\left(\frac{m_s}{m_d}\right)^2 = 1 \tag{2}$$

where the semi-major axis Q is given by the ratio:

$$\mathcal{Q}^2 = \frac{m_s^2 - \hat{m}^2}{m_d^2 - m_u^2} \tag{3}$$

with $\hat{m} = (m_u + m_d)/2$.

One way to determine $\mathcal{Q}$ is by means of a ratio of meson masses:

$$\mathcal{Q}^2 = \frac{M_K^2}{M_\pi^2}\frac{M_K^2 - M_\pi^2}{(M_{K^0}^2 - M_{K^+}^2)_{QCD}}[1 + O(m_{quark}^2)] \tag{4}$$

The major problem in extracting $\mathcal{Q}$ from this relation arises from the uncertainties in the electromagnetic contributions to the $K^0 - K^+$ mass difference. Another way to extract $\mathcal{Q}$ is by means of $\eta \to \pi\pi\pi$ decays that have negligibly small electromagnetic corrections due to chiral symmetry. This second approach thus represents a more sensitive probe of the symmetry breaking generated by $m_d - m_u$, and has the potential to deliver accurate quark mass ratios [11]. As emphasized by Leutwyler [10], the main errors in determining $\mathcal{Q}$ using $\eta \to \pi\pi\pi$ decays is due to the experimental uncertainties in the partial width $\Gamma_{\eta \to \pi\pi\pi}$ that are determined by the two-photon widths $\Gamma_{\eta \to \gamma\gamma}$ and the branching ratio. The two different methods of measuring $\Gamma_{\eta \to \gamma\gamma}$ (photon-photon collisions and the Primakoff effect) yield conflicting results, as shown in figure 1. This is an important example of the impact that the precise measurement of the η two-photon widths would have for determining fundamental parameters of QCD.

In summary, due to a relative larger mass, the η meson represents a sensitive probe for studying QCD symmetries and symmetry breaking at low energy. The spontaneous chiral symmetry breaking gives birth to the η as one of the Goldstone particles and the chiral axial anomaly primarily determines the η lifetime. Due to SU(3) symmetry and isospin breaking, the physical η has mixing components from the eigenstates of the π_8^0, η_8 and η_0. It opens a new window on the determination of fundamental parameters of QCD in a model-independent manner, such as the light quark-mass ratio $((m_u - m_d)/m_s)$ and the mixing angle of η-η'. In addition, precision measurement of radiative η decay width will improve all other η partial decay widths. As a result, precision measurements of the $\eta \to \gamma\gamma$ decay width will have a wide ranging impact on understanding QCD at the confinement scale.
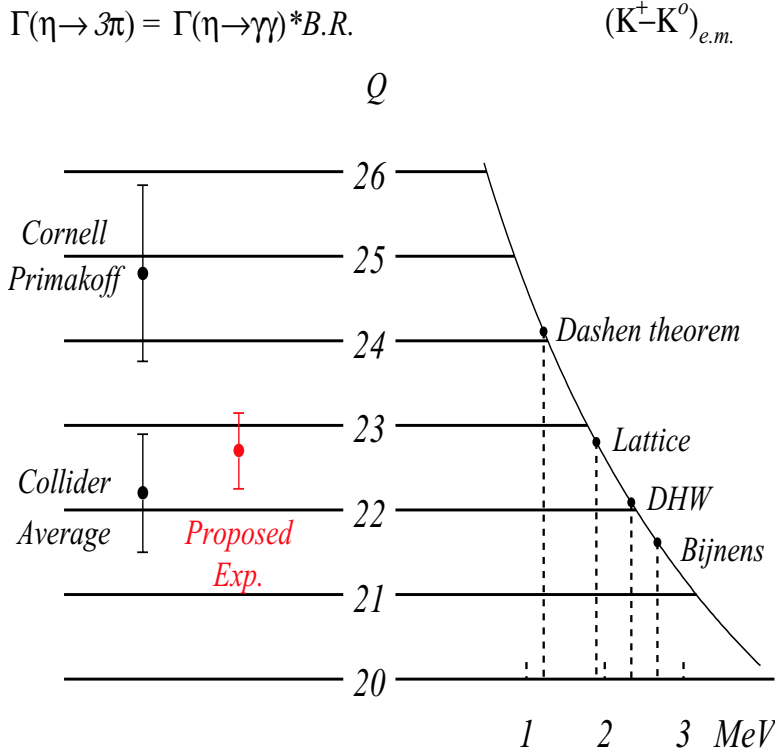
Figure 1: The importance of $\Gamma_{\eta\rightarrow\gamma\gamma}$ in the measurement of $\mathcal{Q}$. The *l.h.s.* indicates the values of $\mathcal{Q}$ corresponding to the Primakoff and collider experimental results for the $\Gamma_{\eta\rightarrow\gamma\gamma}$. The *r.h.s.* shows the results for $\mathcal{Q}$ obtained with four different theoretical estimates for the electromagnetic self energies of the kaons. Taken from Ref. [10].

3 Previous Measurements of the η Radiative Width

The present experimental knowledge of the η meson width is presented in figure 2 [12], along with the projected measurement which could be made with 12 GeV at Jefferson Lab. Most of the measurements in the figure have been performed using two photon interactions in e^+e^- collisions. One exception is the Cornell measurement of the η width [13] via the Primakoff effect. This gives a reported width which is significantly lower (at the 3σ level) than those from e^+e^- collisions. The Particle Date Group had listed both two-photon and Primakoff measurements for more than 30 years in the past due to "no compelling reason"[14] to exclude the Cornell Primakoff result. After more than 30 years without a new Primakoff experimental confirmation, the Cornell result was removed from the Particle Date Group in 2006 following the advice of Nefkens[4]. On the other hand, using the same apparatus, the Cornell group measured the $\Gamma(\pi^0 \rightarrow \gamma\gamma) = 7.93 \pm 0.39$ eV [15], in good agreement with the world average value of 7.74 ± 0.55 eV. From the experimental point of view, the major differences between the Cornell group's π^0 result and their η result are: (1), the resolution of reconstructed meson production angle for the π^0 case was made better than the η case

by doubling the distance between the target and the photon detector (calorimeter), which helps to better discern the characteristic shapes of the different production mechanisms; (2), there is less overlap between the Primakoff production and the nuclear background in the π^0 measurement than the η due to the smaller mass of pion; and (3), the Primakoff π^0 production is peaked at smaller q^2 than the η, making the fit less sensitive to details of charge form factor calculations. As such, the η width should be remeasured by the Primakoff process using state-of-the-art experimental techniques to resolve the discrepancy between the Primakoff and two-photon measurements. The proposed experiment will improve the previous the Primakoff experiment in the following aspects:

1. Improve the η angular resolution by using a high resolution PbWO$_4$ crystal calorimeter;

2. Use a tagged high energy photon beam to control the photon flux;

3. Choose light targets, proton and ^{4}He, and ^{12}C to enable good separation of the Primakoff production mechanism from nuclear background;

4. The charge form factors of the targets, the proton, ^{4}He, ^{12}C and are well known.

4 Measurement of the η Radiative Width via the Primakoff Effect

We propose to use a tagged photon beam in Hall D to measure the width of the $\eta \to \gamma\gamma$ decay via the Primakoff effect. In the Primakoff effect, shown in figure 3, mesons are produced by the interaction of a real photon with a virtual photon from the Coulomb field of the nucleus. The formation of mesons will be identified through the invariant mass of the two decay photons from the $\eta \to \gamma\gamma$ reaction, and the meson production angles will also be reconstructed by detecting the η decay photons.

The production of mesons in the Coulomb field of a nucleus by real photons is essentially the inverse of the decay $\eta \to \gamma\gamma$, and the cross section for this process thus provides a measure of the η two-photon decay widths. For unpolarized photons, the Primakoff cross section on a zero-spin nuclear target is given by[16]:

$$\frac{d\sigma_P}{d\Omega} = \Gamma_{\gamma\gamma} \frac{8\alpha Z^2}{m^3} \frac{\beta^3 E^4}{Q^4} |F_{e.m.}(Q)|^2 sin^2\theta \tag{5}$$

where $\Gamma_{\gamma\gamma}$ is the decay width of the η, Z is the atomic number, m, β, θ are the mass, velocity and production angle of the mesons, E is the energy of the incoming photon, Q is the momentum transferred to the nucleus, and $F_{e.m.}(Q)$ is the nuclear electromagnetic form factor, corrected for final state interactions of the outgoing η.

The Primakoff effect is not the only mechanism for meson photoproduction at high energies. There is coherent background from strong production of η in the nuclear hadronic field, and an interference between the strong and Primakoff production amplitudes. The full cross section is given by:

8

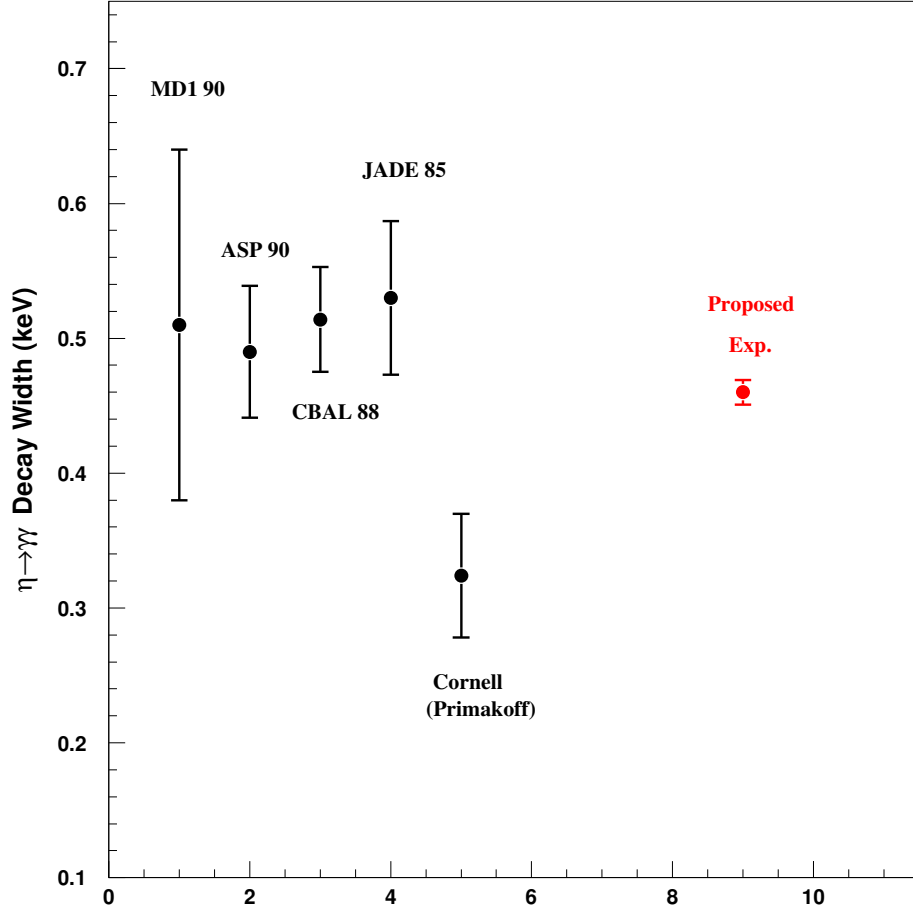Figure 2: Two-photon decay width for the η meson. Points 1 through 4, are the results of e^+e^- collisions (for references, see[12]), point 5 is the result of a Primakoff experiment [13]. Point 6 is the expected error for our future experiment, arbitrarily plotted to agree with the average value of previous five measurements. The plotted uncertainties combine the statistical and systematic errors in quadrature (see table 1).
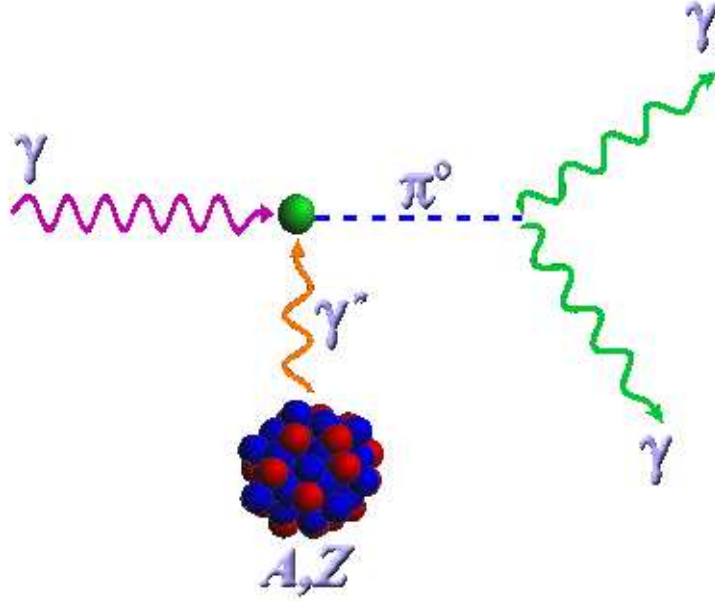
9

Figure 3: Schematic representation of the Coulomb photoproduction of neutral mesons (Primakoff effect).

$$\frac{d\sigma}{d\Omega_\pi} = \frac{d\sigma_P}{d\Omega} + \frac{d\sigma_C}{d\Omega} + \frac{d\sigma_I}{d\Omega} + 2 \cdot \sqrt{\frac{d\sigma_P}{d\Omega} \cdot \frac{d\sigma_C}{d\Omega}} cos(\phi_1 + \phi_2) \qquad (6)$$

where the Primakoff cross section, $\frac{d\sigma_P}{d\Omega}$, is given by equation (5). The nuclear coherent cross section is given by:

$$\frac{d\sigma_C}{d\Omega} = C \cdot A^2 |F_N(Q)|^2 sin^2\theta_m \qquad (7)$$

and the incoherent cross section is:

$$\frac{d\sigma_I}{d\Omega} = \xi A(1 - G(Q))\frac{d\sigma_H}{d\Omega} \qquad (8)$$

where A is the nucleon number, $Csin^2\theta_m$ is the square of the isospin and spin independent part of the neutral meson photoproduction amplitude on a single nucleon, $|F_N(Q)|$ is the form factor for the nuclear matter distribution in the nucleus (corrected for final state interactions of the outgoing mesons), ξ is the absorption factor of the incoherently produced mesons, $1 - G(Q)$ is a factor which reduces the cross section at small momentum transfer due to the Pauli exclusion principle, and $\frac{d\sigma_H}{d\Omega}$ is the η photoproduction cross section on a single nucleon. The relative phase between the Primakoff and nuclear coherent amplitudes without final

state interactions is given by ϕ_1 and the phase shift of the outgoing meson due to final state interactions in the final state is given by ϕ_2.
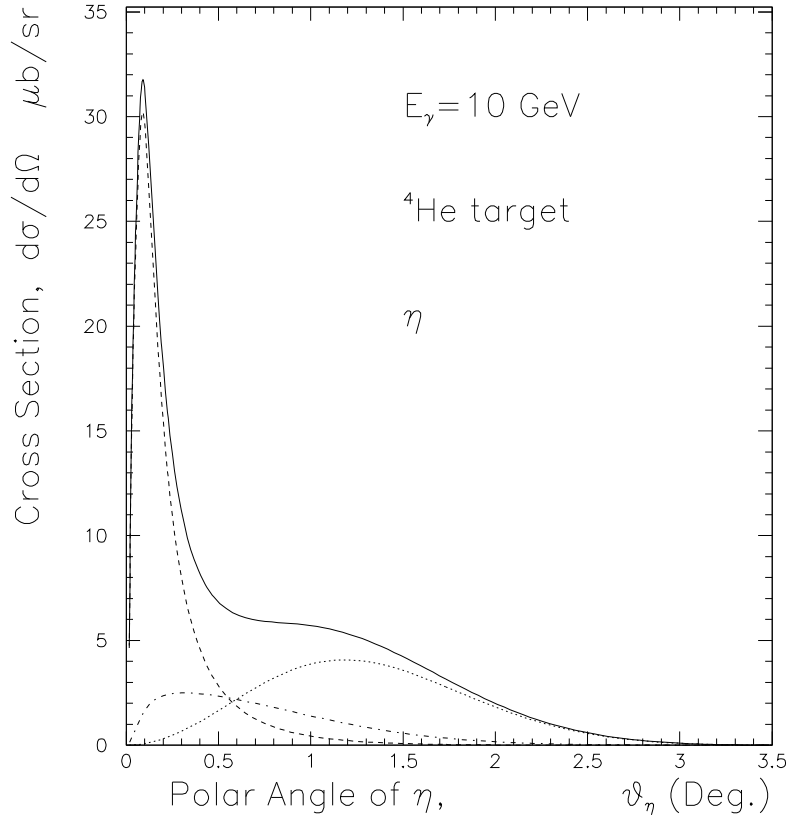

Figure 4: Differential cross sections (electromagnetic and nuclear) for the $\gamma +^4 He \rightarrow \eta +^4 He$ reaction at small angles at 10 GeV. The solid line is the total differential cross section from all the process, the dashed line is from Primakoff process, the dotted line is from the nuclear coherent process, and the dot-dash line is from the interference of the Primakoff and nuclear coherent processes.

The classical method of extracting the Primakoff amplitude from the measured differential cross sections in the forward direction relies on the different characteristic behaviors of the production mechanisms with respect to the production angle. For a spin zero target the Primakoff cross section is zero for mesons emitted along the incident photon direction, has a sharp maximum at a very small angle, and falls at larger angles as shown in figure 4 for a ^{4}He target. It is proportional to Z^2, and its peak value is roughly proportional to E^4. The nuclear coherent cross section for spin zero nuclei is also zero in the forward direction, but it has a broad maximum outside the angular region of the Primakoff effect, and falls at larger angles as shown in figure 4, where the amplitudes are normalized to the Cornell data [13]. However, as can be seen from figure 4, there are still two types of contributions under the

Primakoff peak–the extended tail of the nuclear coherent mechanism, and the interference term between the two amplitudes as described above. The interference term amounts to a relatively large contribution and is also more difficult to identify since in addition to the knowledge of both amplitudes, it also requires knowing the relative phase angle between them. Therefore, a precision determination of the contribution from the background amplitudes under the Primakoff peak requires good experimental information on the nuclear amplitude outside of the Primakoff region. This can be experimentally achieved by using light nuclei as production targets. Since form factors for light nuclei fall slowly with momentum transfer, such targets are well suited for measuring the nuclear part at large angles, thereby determining the contribution under the Primakoff peak.

As figure 4 illustrates, compared to the Primakoff effect to produce a π^0, η production has a significantly smaller cross section and peaks at relatively larger production angles. This is a consequence of the much larger mass of the η which increases the momentum transfer at a given production angle. As a result, the Primakoff peak is harder to distinguish from the nuclear background, as seen from Cornell groups result [13]. There are two ways to ameliorate this problem. One is to go to higher photon energies, which, in addition to increasing the Primakoff cross section ($\sigma_P \propto E^4$), will push the Primakoff peak to smaller angles ($\theta_{Primakoff} \sim \frac{m^2}{2E^2}$) as compared to those of the nuclear coherent effect ($\theta_{NC} \sim \frac{2}{EA^{\frac{1}{3}}}$). As such, the 12 GeV upgrade to the CEBAF accelerator is vital to these measurements. Another improvement is to use lighter targets such as ^{1}H, ^{4}He and ^{12}C, which are more bound compared to heavier nuclei, thereby enhancing coherency. In addition, due to the A dependence just mentioned, one would expect the nuclear coherent mechanism to peak at larger angles for lighter nuclei, which helps to separate it from Primakoff production.

In this proposal we are suggesting a measurement of the differential cross sections at forward angles on three targets: the proton and ^{4}He and ^{12}C. The ^{12}C target was used in our previous π^0 Primakoff experiment and the target thickness is known with a precision better than 0.1%. We plan to use it in the η experiment as well in order to check the consistency. The ^{4}He has several advantages over other targets. First, it is a very compact nucleus (with a nucleon threshold of $\sim$20 MeV), which will favor coherent production. Second, its form factor is very well known and falls slowly with momentum transfer. In addition, it is a spin zero nucleus, which will largely suppress the spin flip amplitude contribution close to zero degrees.

On the other hand, there is a contribution from nuclear incoherent production to the η photoproduction. As a recent article [17] pointed out, the nuclear incoherent contribution should not be isotropic as previously considered in Cornells analysis. A more reasonable interpretation of the incoherent contribution gives $\Gamma_{\eta \to \gamma\gamma} = 0.476$ keV which is about 50% greater than the value of 0.324 KeV obtained by the Cornell group [13]. As a production target, hydrogen is especially promising. For many-body nuclei, there is the complication due to inelastic transitions and breakup channels at low excitation energy, whereas for the proton target it will be possible to guarantee coherency through kinematic cuts. Inspired by the *PrimEx* experiments, the η Primakoff cross section on a proton target has been recently calculated by J. Laget [18]. It should be noted that a proof-of-principle exists for doing a Primakoff experiment on the proton. In the early 1970's a group at DESY measured

forward π^o photoproduction on the proton [19]. Their data clearly exhibit a Primakoff peak at forward angles, and the pion lifetime obtained from the data agrees, within quoted errors, with the accepted value.

We argue that by simultaneously going to higher photon energies and using lighter Primakoff production targets, one can make clean measurements of the η decay width.

5   Experimental Setup

We propose to use a 10.5–11.7 GeV tagged photon beam in Hall D to produce the η mesons, and the two decay photons from the η will be detected by the HYCAL calorimeter located $\sim$ 6.5 m downstream of the target. The experimental setup includes: (1) a high energy photon tagger; (2) a pair spectrometer for photon flux monitoring; (3) physics targets; (4) a high resolution multichannel HYCAL calorimeter; (5) a photon beam position monitoring detector. During the η production run, the GlueX solenoid magnet will be turned off in order to detect the atomic electron Compton scattering events in the calorimeter simultaneously to calibrate and monitor the experimental systematic errors. Details of this instrumentation are given below.

5.1   High Energy Photon Tagger

Jefferson Lab is in the process of designing and developing a tagged photon beam at 12 GeV in Hall D. While details of the design can be found in reference [20], the main features of the current design are:

1. Photon energy detection from 70% to 75% of the primary electron beam energy with energy resolution of about 0.5% r.m.s. A detector system which allows a counting rate of at least 5×10^6 electrons per second per 0.1% over this range of photon energies.

2. An additional capability for photon energy detection from 25% to 97% of the primary electron beam energy. It will be capable of pre-collimated intensities up to 150MHz/GeV, with 50% sampling of 60 MeV energy bins below 9 GeV and full coverage with 100% sampling of 30 MeV wide energy bins above 9 GeV photon energy.

The tagging spectrometer is an Elbek-type spectrometer. The 12 GeV electrons pass through the radiator target where a small fraction undergo bremsstrahlung. The electrons then pass through a focusing quadrupole and are bent by the $6.3m$ tagger magnet. The majority of the electrons which did not interact with the radiator are bent 13.4° and then propagate straight to the electron beam dump. A large vacuum vessel is integrated into the magnet and extends out to the spectrometer focal plane so only the small amount of multiple scattering inside the radiator and in the exit window effect the resolution. The spectrometer detectors are positioned immediately outside the focal plane to determine the momentum of electrons that produce bremsstrahlung photons. The photon energy, E_γ, is determined by the difference between the initial electron beam energy and the energy of the post-bremsstrahlung electron deflected towards the focal plane.

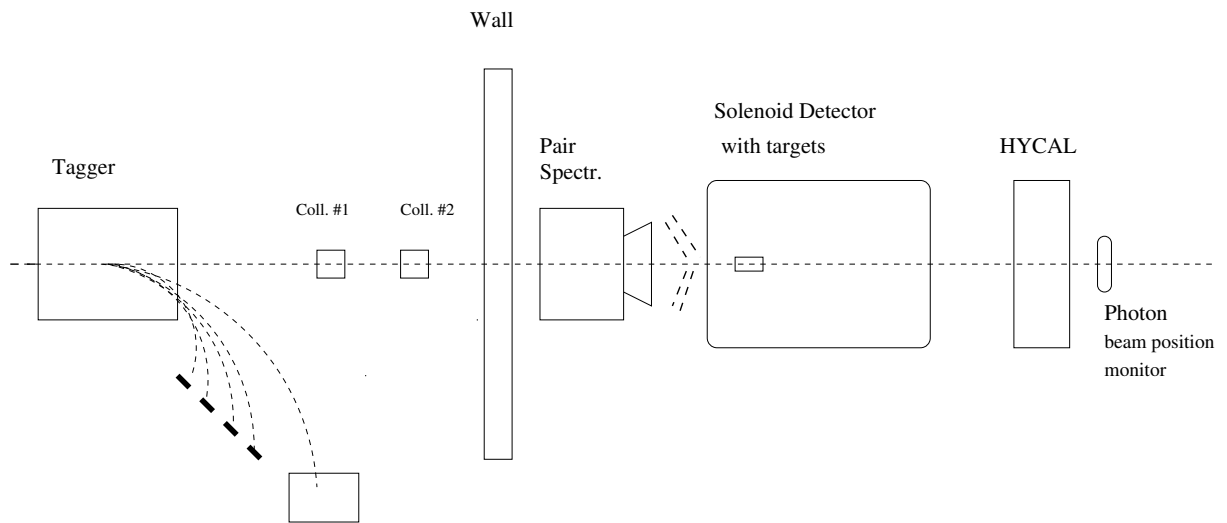Proposed Experimental Setup

Standard Hall D/GlueX setup with HYCAL

Wall

Solenoid Detector
with targets

Pair
Spectr.

HYCAL

Tagger

Coll. #1   Coll. #2

Photon
beam position
monitor

Figure 5: Top view of the experimental setup for η two–gamma decay width measurements. It includes: (1) a high energy photon tagger; (2) a pair spectrometer; (3) physics targets; (4) the HYCAL calorimeter; (5) a beam position monitoring detector.

The detector package is divided into two parts: (1) a set of 190 fixed scintillation counters spanning the photon energy range from 3.0 to 11.7 GeV, and (2), a movable "microscope" of 500 scintillating fibers optimized for coherent photon beam operation spanning the energy range from 8.3 to 9.1 GeV. The fixed array provides access to the full tagged photon spectrum, albeit at a modest energy resolution of 0.5% and reduced rate capability. These detectors are well suited for running with a broadband incoherent bremsstrahlung source. The microscope is needed in order to run the source in coherent mode at the highest polarization and intensities, and whenever energy resolution better than 0.5% is required. Using the microscope, the source is capable of producing collimated photon spectral intensities in excess of 2×10^8 photons/GeV, although accidental tagging rates will limit normal operation to somewhat less than this.

For the proposed η radiative decay width measurement, we will use an incoherent bremsstrahlung photon beam in an energy range from 10.5 GeV to 11.7 GeV. The current design of the fixed scintillation counters in this energy range with 30 MeV wide energy bins is sufficient for this measurement.

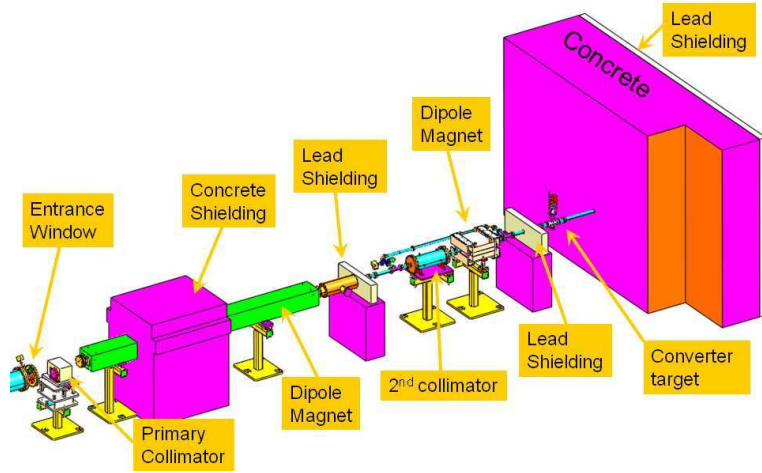**Beam Collimation and Position Stability**

Figure 6: The layout of the collimator cave.

A 12 GeV electron beam interacting with a 20 μm diamond radiator will produce a photon beam. The characteristic opening angle for bremsstrahlung photons is $m_e/E = 42$ μrad. After 76 meters of drifting in vacuum the photon beam enters in the collimator cave from the left through a thin 250 μm Kapton window 8″ (203mm) in diameter and immediately interacts with the primary collimator. The layout of the collimator cave is shown in figure 6. The primary collimator consists of two main components: an active collimator which measures the centroid of the photon beam and a hybrid tungsten lead passive collimator. The size of passive collimator is 3.4mm in diameter for the GlueX run, however, we will use a larger collimator size of $5mm$ in diameter for η decay experiment in order to double the photon tagging efficiency. The active collimator is electrically isolated, has an inner aperture of $5mm$, and is precisely mounted in front of the primary collimator.

The purpose of the active collimator is to measure the position of the centroid of the photon beam with an accuracy of 200 μm. The tungsten passive collimator is surrounded in 8″ of lead for additional shielding. A large flux of particles are generated in the passive collimator and some lie along the photon beam. A sequence of sweeping magnets is after the collimation to remove the unwanted particles from the photon beam. A second collimator is located following the lead shielding wall of the first collimator. This collimator is made of stainless steel and is 20″ long and 8″ in diameter. A $1cm$ hole is bored along the axis of the collimator and it is designed so that the effective aperture can be adjusted to 6, 8, or 10 mm by inserting stainless steel tubes in the collimator aperture. The purpose of this collimator is to scrape off photons which were produced by low angle scattering on the bore of the primary collimator. A second sweeping magnet is mounted directly after the second collimator.
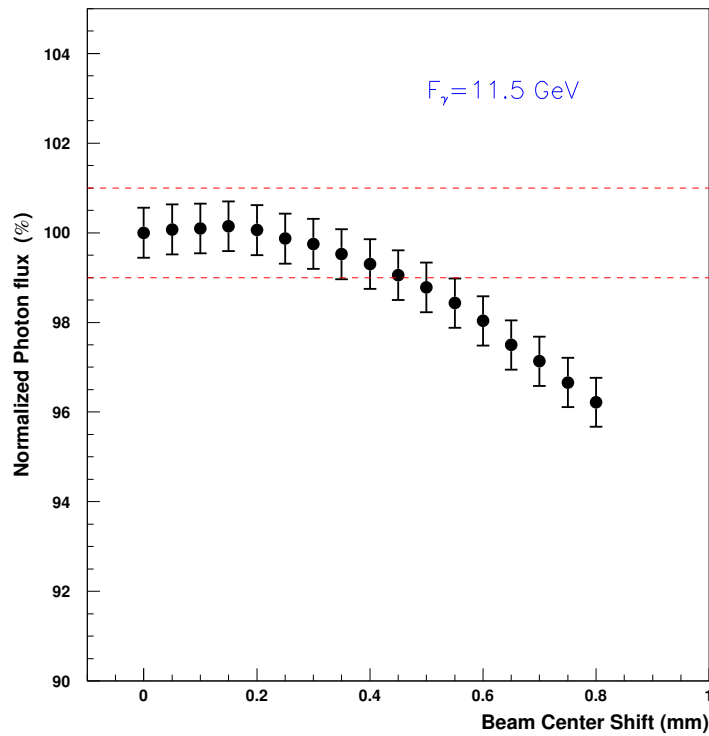

Figure 7: Results from Monte Carlo studies of photon flux stability for a $5mm$ diameter primary collimator. It shows the normalized photon flux after the collimation as a function of the offset of the beam centroid from the collimator axis. The dashed lines show $\pm 1\%$ deviation from the photon flux when the beam centroid has a zero offset.

The specification of the tolerance on this alignment during beam operation is a circle of radius 200 microns. The size of the beam spot on target is defined by the primary collimator. As shown in figure 7, if the beam centroid is aligned within 200 microns, the deviation of the photon flux on the target can be controlled within 1% for a $5mm$ in diameter primary collimator.
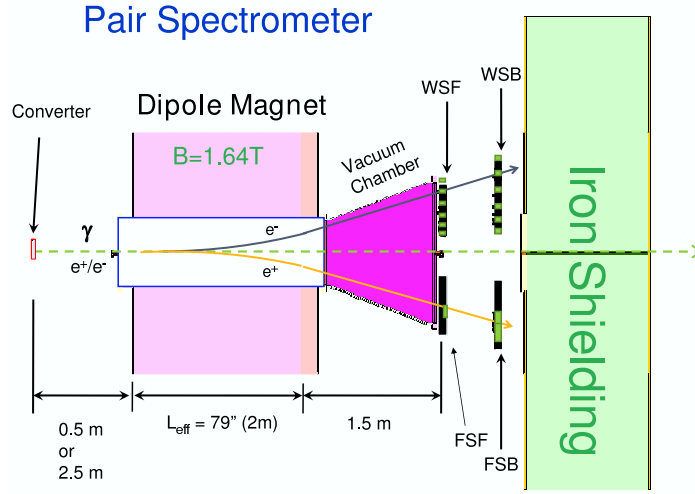
16

5.2 Pair Spectrometer

Figure 8: Layout of the pair spectrometer in Hall D. On the left is a thin 10^{-3} radiation length converter followed by a strong spectrometer magnet. The vacuum chamber extends beyond the end of the magnet to the front of the first hodoscope plane. The first scintillator hodoscope is placed 1.5 m beyond the end of the magnet. A second hodoscope plane is placed 0.8 m behind the first plane and is used for triggering.

The most important diagnostics for the photon beam flux are the count rates in the tagger's fixed hodoscope array and the microscope. By detecting the electrons which underwent the bremsstrahlung interaction, one determines precisely the energy spectrum of the photon beam in front of the collimators. The photon flux on the target, however, is only a fraction of the tagged photons because of the collimation. The absolute photon flux on the target will depend strongly on the exact details of the collimation. It is proposed to use pair production which is a well understood QED process as the basis for the relative photon flux determination. An additional calibration measurement is needed to determine the pair spectrometer's absolute efficiency. This is done with dedicated calibration runs at low beam intensity with a total absorption counter (lead glass) inserted in the beam after the spectrometer.

The layout of the proposed pair spectrometer is shown in Figure 8. It consists of a thin foil converter (1×10^{-3} radiation length thick) placed in the photon beam after the last collimator (0.5 m or 2.5 m before the front end of the pair spectrometer magnet) to generate electron/positron pairs through pair production. The electrons and positrons produced in the converter are swept away from the photon beam in a strong dipole field (1.64 T) and are subsequently detected in scintillator hodoscopes placed 1.5 m (front arrays) and 2.3 m (back arrays) after the magnet in coincidence. The photon energy is then simply the sum of the electron and positron energies.

The pair spectrometer detector package has asymmetrical design and consists of a total of

42 counters. On the positron side the Fine Spacing Forward (FSF) hodoscope will consist of 24 close packed scintillator counters measuring momenta between 3 and 4 GeV/c in equally spaced momentum bins. The momentum uncertainty per bin is 12 MeV. On the electron side the Wide Spacing Forward (WSF) hodoscope is a sequence of six narrow scintillators covering the range 3.25 to 8.25 GeV/c. The momentum uncertainty per bin is 17 MeV. There are an additional four Fine Spacing Backward hodoscopes (FSB) in the positron arm and six Wide Spacing Backward hodoscopes (WSB) in the electron arm used for triggering purposes. A coincidence between one counter in the FSF and one in the WSF corresponds to one photon energy bin. This arrangement gives $6 \times 24 = 144$ photon momentum bins equally spaced in energy between 6.25 GeV and 12.25 GeV with a nominal 21 MeV uncertainty per bin. This spectrometer design provides uniform acceptance over the energy range from 6.25 GeV to 12.25 GeV using a minimum number of counters. The detailed design can be found in reference [20].

The proposed η experiment will use the incoherent photon beam at the highest possible energy (E_γ=10.5–11.7 GeV). For a 1×10^{-3} thick converter, 2.2 μA electron beam on a 20 μm thick diamond radiator, and a 5 mm diameter primary collimator, Monte Carlo simulation indicates that there will be about 5-10Hz coincidence rate per photon momentum bin on the pair spectrometer for the bremsstrahlung energy from 10.5 GeV to 11.7 GeV. This will allow us to control the photon flux at the 1% level.

5.3   Targets

We propose to use three targets in this experiment: liquid hydrogen, liquid helium and a natural isotopic carbon target. The thicknesses of the hydrogen, helium and carbon targets are approximately 30 cm, 30 cm, and 1 cm, respectively, corresponding to radiation lengths of approximately 3.4%, 4.0%, and 5.0%. Details of the targets are given in the following sections. In brief, we believe that it will possible to hold the uncertainty in the area density, atoms/cm^2, of the targets to the level of $\pm 0.16\%$ for the cryogenic hydrogen and helium targets, and to the level of $\pm 0.05\%$ for the carbon target.

Liquid Hydrogen and Helium Targets

Hall D is planning to use a cryogenic target system similar to what has been developed for Hall B[21]. A few details of the Hall D target system are still undefined, most notably the source of cryogenic helium for liquefying the target gases. Options include (i) using cryogenic helium from the CEBAF central refrigeration system, which supplies helium at 5K and three atmospheres pressure (not convenient because of the high pressure), (ii) drawing low pressure 4.5K liquid helium from a port on the Hall D magnet (the Hall B target works this way, drawing helium from the torus), or (iii) use a separate refrigerator for the target. Independent of the source of the cryogenic helium, the main element of the cryogenic target is a heat exchanger in contact with the target that is refrigerated down to 2.5K by pumping liquid helium through a Joule-Thompson valve. Experience in Hall B has shown that after a 15-liter buffer cryostat has been filled from the torus, oscillations in the target temperature are smaller than $\pm 0.02 K$[22].

During the experiment, target temperatures and pressures will be written into the data stream. Since target vaporization does not occur for incident real photon beams, unlike for electron beams, the target density can be deduced from the hydrogen/helium equations of state and the target pressure-temperature data. This has been performed in detail for the CLAS G1C run period, and the uncertainties in the average hydrogen densities for G1C runs taken at the same beam energies were estimated at $\pm 0.14\%$ [23].

A photograph of a Hall B g10a target cell, with design similar to that proposed for use in Hall D, is shown in figure 9. This cell is $24cm$ in length, and the upstream end of the target has an inner diameter of $5.51cm$, tapering down to $4.0cm$ inner diameter on the downstream end of the target. The reason for the tapering is to eliminate dead zones in the target, where cooling is limited. The radius on the endcaps is $4cm$. The target cell is constructed from $5mil$ kapton.

Figure 9: Photograph of the CLAS g10a target.

The curvature on the target endcaps can potentially cause a significant uncertainty in the effective length of the target, since the effective target length depends on the photon

spot size, and the target offset and angle relative to the beam. These effects were carefully studied for the CLAS G1A run period [4]. In the G1A analysis the largest systematic error in the effective target length was estimated to result from an offset of the target from the scattering center. In the early days of Hall B running the target offset was estimated to be as large as $5mm$. This caused a systematic uncertainty in the effective target length of $1mm$ for G1A running.

To make an estimate for the uncertainty in the effective target length for the Hall D experiment, we made the following assumptions:

- Target length of $30cm$, with endcap radius of $4cm$.

- Beam spot sigma of $1.5mm$ ($5mm$ collimation $20m$ from the target)

- Target-center offset no greater than $1mm$

- Target-front offset from target-back no greater than $1mm$

If the target offsets can be held to the level of $1mm$, then the uncertainty in the effective target length is dominated by the uncertainty in measuring the target length, which is estimated at $\pm 0.2mm$ [24]. This gives a fractional error in the effective target length of $\pm 0.07\%$.

To summarize, during the experiment we propose to carefully monitor the cryogenic target pressures and temperatures, and continually write these variables into the event stream. Based on experience running similar targets in Hall B, we expect that the target density can be monitored at the level of $\pm 0.14\%$. The target position should be surveyed in with a precision of $\pm 1mm$, giving an error of $\pm$ 0.07% for the effective target length. With these conditions, we estimate that the total uncertainty in the cryogenic target area density can be held at the level of $\pm$ 0.16%.

HOPG (carbon) Target

The carbon target is approximately $380mil$ thick (5% r.l.) and uses Highly Ordered/Oriented Pyrolitic Graphite (HOPG) as the target material. It was machined from a block of HOPG obtained from SLAC. HOPG is produced using high temperature (3273 K) Chemical Vapor Deposition (CVD) furnace technology. This process creates atomic layers of carbon oriented to each other in a crystalline form. One advantage of this process is the very low porosity of the material, 1% as compared to normal graphite's 10% porosity. A piece of the HOPG material was sent away for an elemental analysis using (i) Optimum Combustion Methodology, which detects C, H, N, and O, and (ii) PIXE analysis, which detects 72 heavier elements.

A micrometer with precision of ± 0.05 mils was used to make a map of the thickness of the HOPG target. Figure 10 shows the micrometer map points, and the measured thicknesses in the central region of the target are also shown. The thickness varies by approximately 0.04% over the central region of the target.

The mass density of the HOPG material was measured using the water immersion technique. HPLC grade H_2O was used, which is submicron filtered, packed under inert gas, and has a maximum limit of impurities at 1 ppm. Corrections were made for the temperature

Figure 10: Thickness map of the HOPG target. Units are mils.
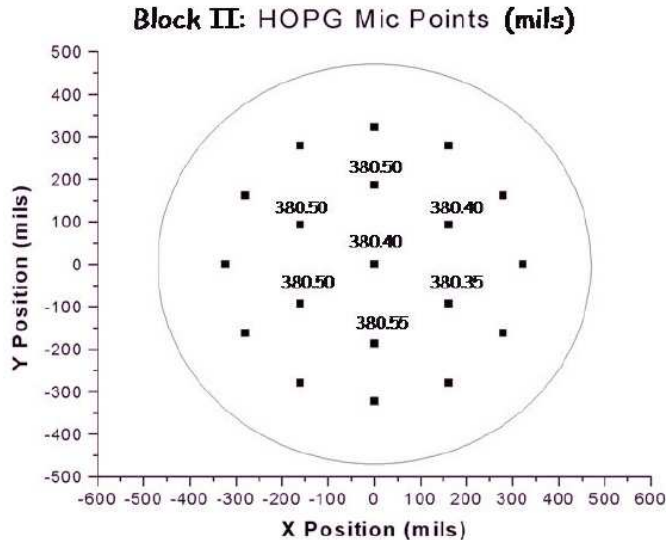
dependence of the water density. A micro-gram scale was used to weight the target block in air and in the water. The mass densities of two identical HOPG blocks were measured three consecutive times, and the results are shown in figure 11. The HOPG mass density used in calculating the areal density of the target was the average of the first five measurements (trial #6 was excluded), and the error in the mass density is taken from trial #3.

Two corrections were applied to density×length to obtain the effective area-density of the target. The first correction is for impurities in the target, which can produce neutral pions through the Primakoff process. The second accounts for the attenuation of the incident photon beam in the target. The NIST XCOM data base was used to calculate the effect of incident beam absorption. Magnetic Primakoff production from ^{13}C is very small compared to Coulomb Primakoff production, and can be neglected. The final result for the effective number of ^{12}C atoms/cm^2 in the target is: $N_{eff}(Z = 6) = 1.0461 \times 10^{23} atoms/cm^2 \pm 0.05\%$.

5.4   Photon Beam Position Monitor

The *PrimEx* collaboration has constructed a photon beam position detector that provided continuous real time photon beam position and profile information during the first experiment, as well as information in the data stream for off-line data analysis. This detector consists of two identical modules crossed at right angles to each other (as shown in figure 12) to give the beam profile along both x and y directions. Each module is a linear hodoscope of multi-channel Bicron scintillating fibers (the x module has 61 channels and the y module has 62) forming a plane perpendicular to the photon beam. This detector is mounted on a remotely controlled table with x and y motion placed just behind the calorimeter in the nominal beam path. Each scintillation fiber has dimensions of $2 \times 2 \times 13$ mm^3. The scintillating light from the fibers is transmitted through the light guide and is detected by
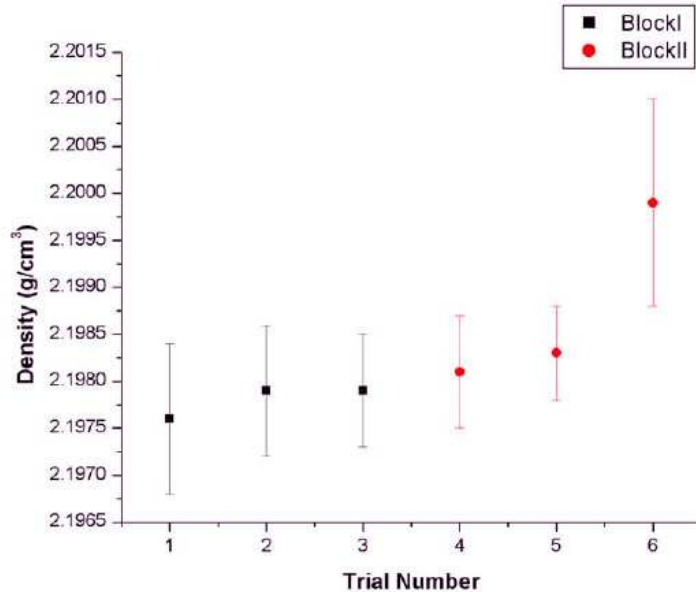
Figure 11: HOPG density measurements.

four 16-channel R5600-M16 Hamamatsu PMTs. A compact electronics module provides 64 channels of amplifier and discriminators for anode signals, then converts them to ECL readout through a time-over-threshold circuit. The ECL signals are sent over to SIS3801-256-flat scalars and read into the EPICS system. During the run, the x and y beam profiles were displayed through a GUI for on-line beam control (shown in figure 13) and read into the DAQ for off-line analysis. This device performed well during the π^0 experiment in Hall B and provided an excellent beam diagnostic tool.

5.5 High Resolution Electromagnetic Calorimeter

5.5.1 Charged Particle Veto

The veto counter system that we propose to use in the Hall D experiment was constructed for the *PrimEx I* experiment. The veto system consists of twelve scintillation paddles with dimensions $120 \times 10 \times 0.5 cm^3$ which cover the front face of the calorimeter. The purpose of the veto counters is to reject charged particle backgrounds incident on the calorimeter. They should have good efficiency for charged particle detection, and be sufficiently thin so that the probability for photon conversion in the paddles is small. The paddles and light guides were built by Saint-Gobain. Light is collected from both ends of the paddles using XP2262B PMTs from Photonis and the tube bases came from Vorg Electronics. The time difference between light propagation times to the two PMTs is used to find the longitudinal coordinate (y) of the hit. The counters are wrapped with an inner layer of Tyvek, and an outer layer of black Tedlar.
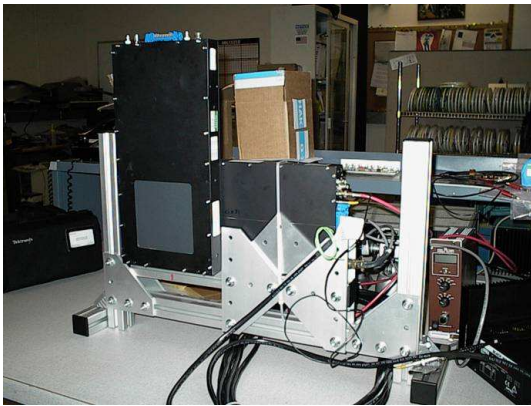
22

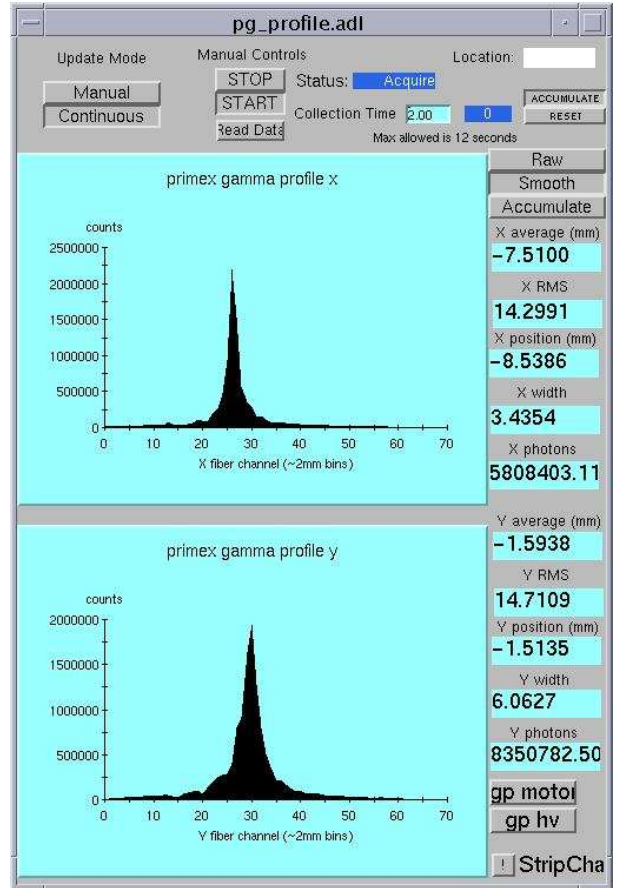Figure 12: The *PrimEx* photon beam position detector.

Figure 13: Photon beam position on-line display.

During the *PrimEx I* experiment, the PMT gains were matched using special runs where e^+e^- pairs produced at the target were swept into the veto paddles by the pair spectrometer magnet, and we propose to take similar data during a Hall D run. The time-walk effects due to varying signal sizes were observable, but were found to be small and had little effect on the y-position resolution. The veto y-positions, which were calculated from the time difference between the top and bottom PMTs, were calibrated against the hit positions given by HYCAL. The average resolution was determined to be $\pm 4.5 cm$, which is within the tolerance of the experiment and corresponds to the width of the counters.

The pair production runs were also analyzed for the charged-particle efficiency. The efficiencies were determined by dividing the number of particles detected by a veto counter by the number of particles detected in the region of HYCAL covered by the acceptance of the given veto. Figure 14 (left) shows that the charged-particle efficiency for the veto counters is approximately 95%.

For the neutral misidentification analysis, data with low intensity photon beams incident on each veto counter were utilized. Figure 14 (right) shows the neutral misidentification probability for the counter at $x = -15 cm$ *versus* the y-position given by HYCAL. The
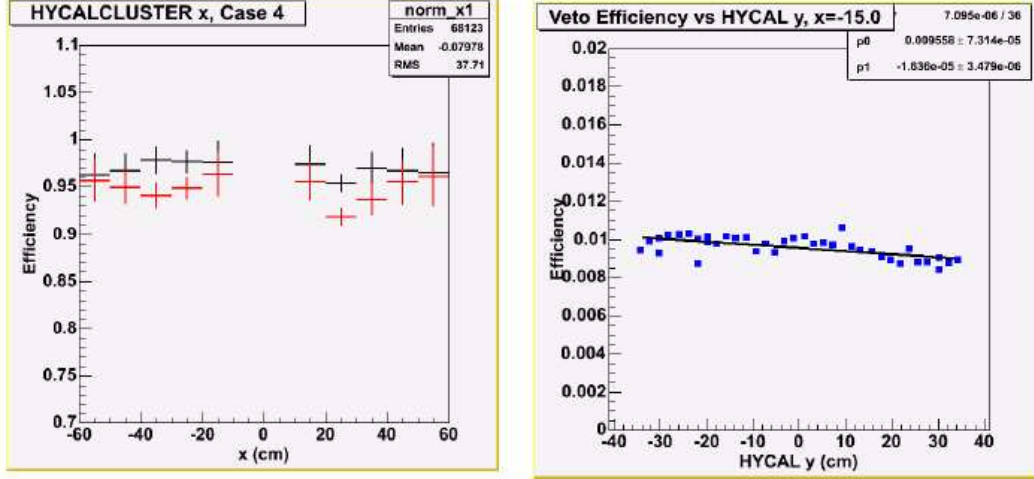
23

Figure 14: Left: Charged-particle detection efficiency. The black points are from matching the veto counters with HYCAL by x-position and timing. The red data have additional matching in y-position. Right: Neutral particle misidentification probability for veto counter centered at $x = -15cm$ as a function of y. The black line is a linear fit.

plot shows that the conversion probability is low (approximately 1%) and constant over the length of the counter. The other eleven counters show similar results.

Figure 15 shows hybrid mass distributions of neutral pions taken during the *PrimEx I* run with the veto cut not applied, and then applied. The hybrid mass is a weighted sum of the two-photon invariant mass and the elasticity of the event, where the weighting is chosen to optimize the resolution for elastic π^o events. In applying the veto cut, there was a requirement that the veto $x - y$ coordinate should match the hit position in HYCAL, and also that there is a timing correlation between the veto counter and HYCAL. The plots are at π^o angles which range from the Primakoff peak to the nuclear coherent region. The figure shows there is a significant reduction in the background under the π^o mass peak when the veto cut is applied at low angles.

In the *PrimEx I* analysis, a global average derived from the π^o analysis was used to account for photon conversion in the veto counters. Two techniques were developed to obtain the global averages. The first technique involves integrating the hybrid mass distributions, examples of which are shown in figure 16, without and with the veto cut applied. The percent deviation with the veto cut applied is plotted as a function of angle in the top-left plot of figure 16. Note that figure 16 indicates the veto has a progressively weaker effect on the hybrid mass distributions, and this is borne out in the top-left plot of figure 16, where the veto effect asymptotically approaches 0.86% at large angles. The second approach involves finding the number of events in the hybrid mass peaks without and with the veto cut applied. The percentage difference as a function of angle is plotted on the top-right plot of figure 16, and those data points are summed into a histogram on the bottom-right plot of figure 16. From this distribution, the average veto conversion effect on the π^o analysis is estimated at 0.85%, which is in good agreement with the first method.
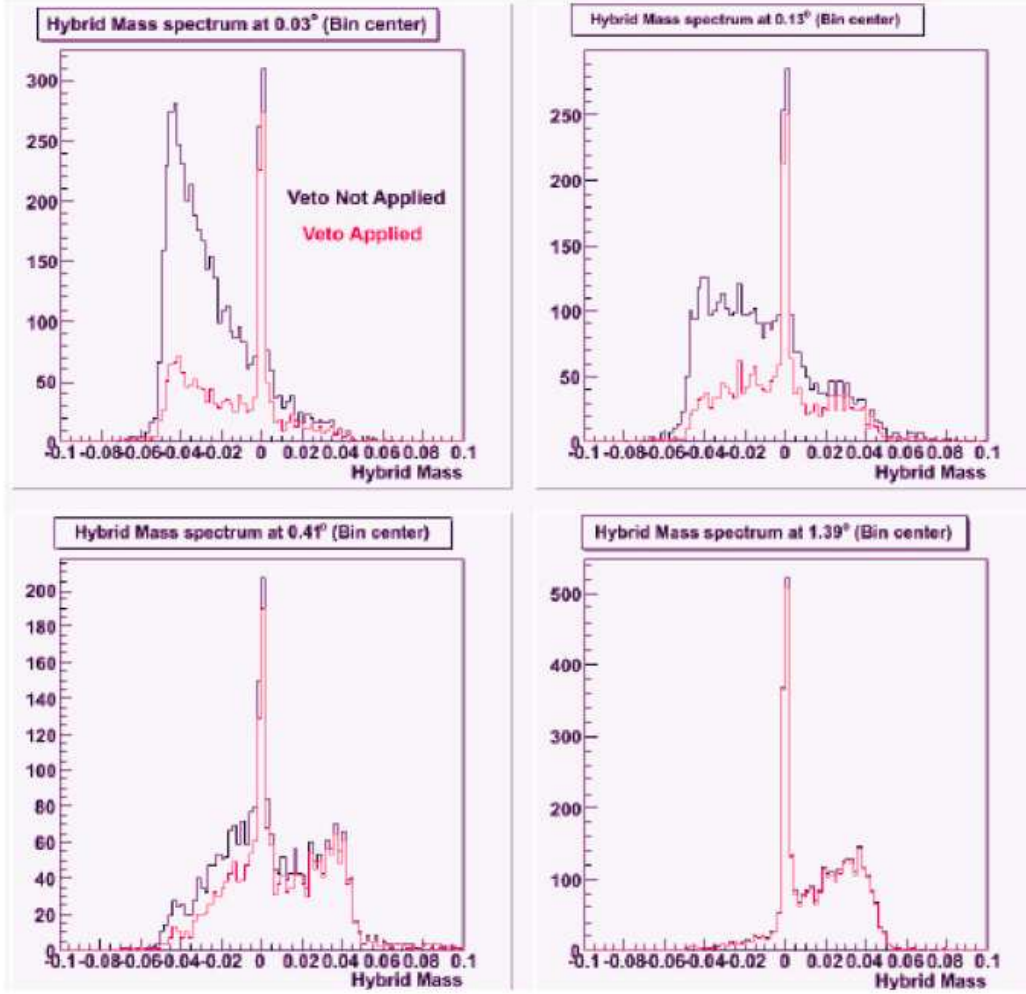
24

Figure 15: Pion hybrid mass spectra at angles of 0.0°, 0.13°, and 1.39° without a veto cut (black), and with a veto cut (red).

5.5.2 The HYCAL Electromagnetic Calorimeter

At the incident photon energies of this experiment (E_γ=10.5–11.7 GeV), the Primakoff cross section peaks at extremely small angles ($\theta_{peak} \simeq 0.2°$). Therefore, in order to extract the Primakoff amplitude from the competing nuclear background, the experimental setup must have sufficient angular resolution for detecting forward produced η's which are identified by detecting the decay photons ($\eta \to \gamma\gamma$) in the multi-channel electromagnetic calorimeter. Good invariant mass resolution in the $\gamma\gamma$ system is also required for the selection of η's from the experimental background. These kinematic variables have strong dependence on both the position and energy resolutions of the calorimeter. In addition, the kinematic constraints imposed by the knowledge of the initial photon energy provided by the tagging system results in a significant improvement of the angular resolution and invariant mass. The combination of the photon tagging facility and high resolution calorimetry is one of the
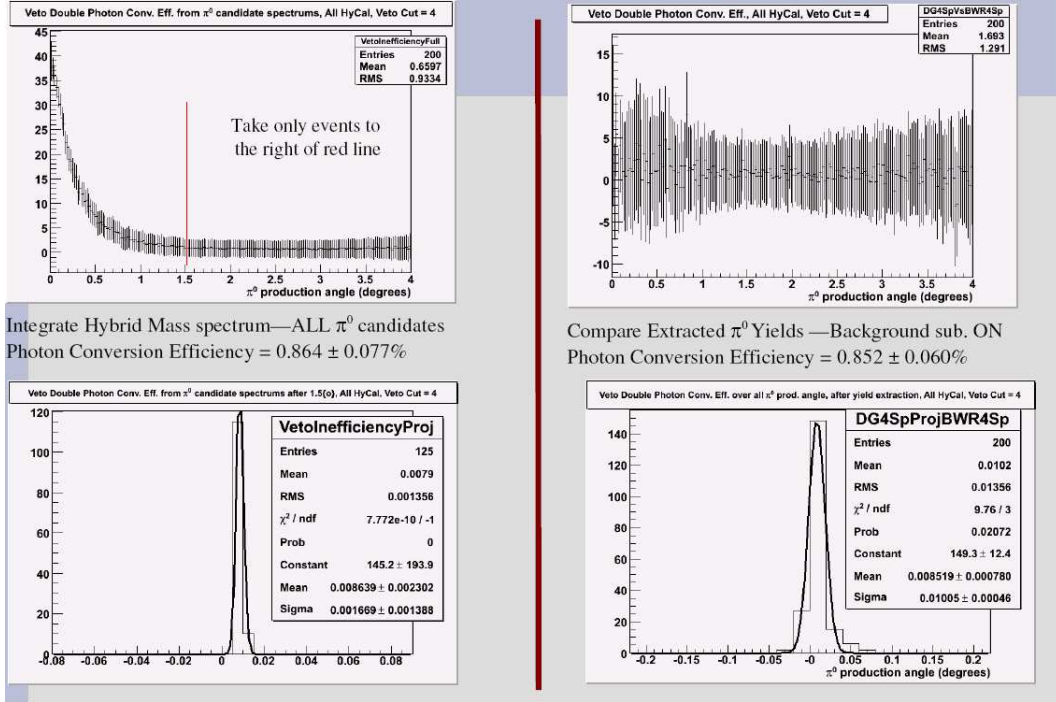
25

Figure 16: Measuring the veto counter photon conversion efficiency for π^o events.

important advantages of our experiment over the previous Primakoff type of experiments. It provides significantly improved invariant mass resolution for the clean identification of the η's and a high resolution in the η production angle for extracting the Primakoff amplitude from the competing background nuclear processes.

In the past several years, a state-of-the art, highly segmented Hybrid Calorimeter (HY-CAL) was developed and constructed by the *PrimEx* collaboration for the π^o lifetime measurements in Hall B. It has been used for the *PrimEx I* experiment in 2004 and will be used in the *PrimEx II* experiment scheduled for 2012. We plan to use the same calorimeter for the proposed η experiment in Hall D. This calorimeter is about 118×118 cm^2 in size. It is designed to measure both the position and the energy of electromagnetic showers using a two dimensional matrix of radiators. The transverse dimension of the individual counters is small enough so that the energy leakage into adjacent counters can be used to determine the position of the shower axis. To optimize the performance and cost, the calorimeter is a hybrid design consisting of two types of detectors (1152 $PbWO_4$ scintillating crystals in the central region and 576 lead glass channels in the surrounding area). There are four distinct 6×24 arrays of lead glass sectors in the outer part of the calorimeter to have a large acceptance. Each counter is TF-1 GAMS-type lead glass Cherenkov detector with dimension $38.2 \times 38.2 \times 450$ mm^3. Each lead glass module was wrapped in aluminized Mylar and viewed with FEU-84 PMT's. For enhanced position and energy resolutions, the central region of the calorimeter is constructed from a 34×34 array of lead tungstate scintillator crystals ($PbWO_4$). Each channel has dimension of $20.5 \times 20.5 \times 180$ mm^3. The scintillation light from the electromagnetic shower was detected with Hamamatsu R4125HA photomultiplier

tubes coupled to the back of the crystals with optical grease. This crystal insertion also significantly improves the radiation hardness of the detector near the beam line where radiation doses are higher. A central 4.1×4.1 cm^2 hole is left open to enable the photon beam to pass through. Each calorimeter module is coupled to a photomultiplier tube (PMT) with optical grease. To optimize the shower leakage in the transition region, the lead tungstate detector assembly is shifted downstream of the lead glass modules by $10cm$. All individual detector modules were stacked in a specially designed light-tight iron frame, as shown in Figure 17. Since the light yield of the crystal is highly temperature dependent ($\sim 2\%/°$C), the detector assembly was surrounded by thick copper plates with circulating coolants. Temperature stability at the level of $\Delta T = \pm 0.1°$C was achieved during the entire period of data collection (three months) in 2004.

The calorimeter is furnished with rear end readout electronics, with signal cables (two from each channel, for anode and dynode signals), high voltage cables and fiber optic cables to the front part of the calorimeter for the gain monitoring system. After 300 ns delay, the anode signals were digitized by means of a 14-bit charge-sensitive ADC (LeCroy 1881M, integration width=240 ns). The positive dynode signals ware summed group by group to form a total sum from the entire calorimeter for the trigger organization.
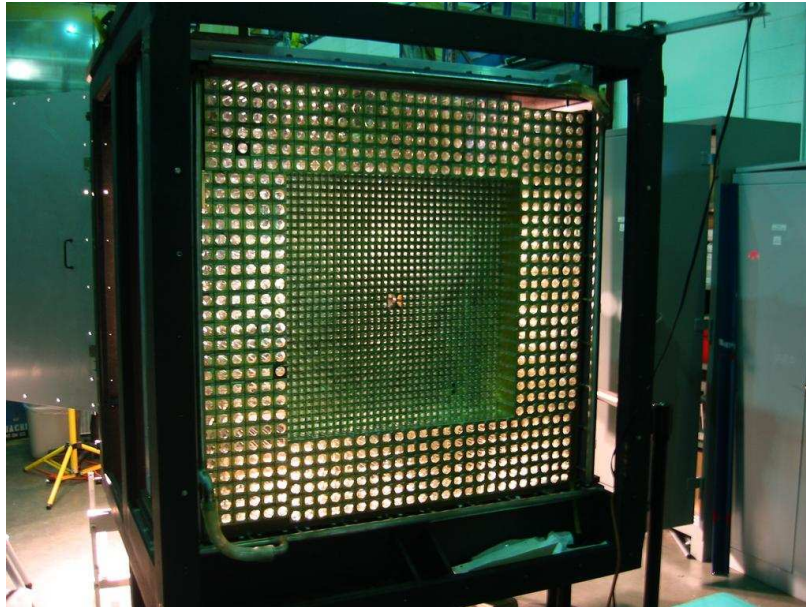

Figure 17: Front view of the HYCAL Calorimeter with all modules in place and before installation of fiber optic cables on front of each channel for the gain monitoring system.

The individual modules of the HYCAL are assembled in a rectangular box inside of the calorimeter frame with total weight of over five tons. The transporter was designed and constructed to provide movement of the entire assembly of the support frame with detectors and thermo-stabilization system, delay cables and gain monitoring system mounted on the bottom of the HYCAL frame and the veto counters on the front of the HYCAL. It is remotely movable in x and y directions with an accuracy of $\pm 2mm$ in order to place each module

in the beam for energy calibration. This system also provides the capability to move the detector along the beam line for different z-positions from the physics target. When the calorimeter is not being used in the beam, the transporter system provides positioning of the entire calorimeter a few meters above the beam center, on Level 2 of the Hall B beam line. In addition to storage, this configuration allows the HYCAL to be available for re-assembly, maintenance, and testing with cosmic rays.

Since there is no sweeping magnet infront of the calorimeter for proposed *eta* experiment in Hall D, we plan to have larger size of central hole ($\sim 6.15 \times 6.15$ cm^2) for the beam and pairproduction background pass through.

5.5.3 Performance of the Calorimeter

The reconstructed energy distribution for the 4.3 GeV electrons from a 2001 beam test with $PbWO_4$ prototype detector is shown in figure 18 for three different calibrated ADC sums: the central module; the inner section comprising 3×3 crystals and the array of 6×6 crystals. The energy resolution is obtained using a Gaussian fit of the 6×6 distribution. As can be seen from the figure, an excellent energy resolution of $\sigma_E/E = 1.3\%$ has been achieved for 4.3 GeV.

During the *PrimEx I* experiment in 2004, the calibration of the HYCAL was performed with a low intensity tagged photon beam of selected energies ($E_\gamma = 0.5-5.5$ GeV), irradiating the centers of each detector module. Then, a tagged photon beam was scanned across the boundary with $2mm$ step size to get data for the position and energy resolutions for the both type of detectors, as well as for the transition region between them. The measured energy resolution *versus* initial photon energy is shown in figure 19. The resolution of the lead glass part of detector is shown in figure 20.

Using the data from the transition region, the energy resolution of the shower cluster was extracted as a function of position. Dependence of the energy resolution *versus* photon impact position is shown in Figure 21. Degradation in resolution as the photon beam passes from the last lead tungstate module to the lead glass region is evident and well described by the Monte Carlo simulation. Figure 21 (bottom) shows the relative reconstructed total energy for the same transition region. The $\sim 3\%$ dip at the interface predominantly arises from shower leakage from the uncovered backs and sides of the lead glass blocks.

The impact coordinates of the electromagnetic particles incident on the segmented hodoscopic calorimeters are determined from the energy deposition of the electromagnetic shower in several neighboring counters. In the case of the $PbWO_4$ crystals, the transverse size of the shower is about two times smaller than that in lead glass. As a result, the position resolution in the $PbWO_4$ detector with an optimal cell size should be about twice smaller than that of lead glass detectors. To maximize the position resolution, we have optimized the crystals' transverse dimensions, and have selected them to be 2.05×2.05 cm^2. This size is comparable to the Molière radius (2.2 cm) of the crystal material.

The distribution of the reconstructed coordinates for 4.3 GeV electrons hitting a crystal cell boundary is shown in Figure 22. The linear dependence of the reconstructed coordinates obtained from a logarithmically weighted average of the cell signals *versus* the impact posi-
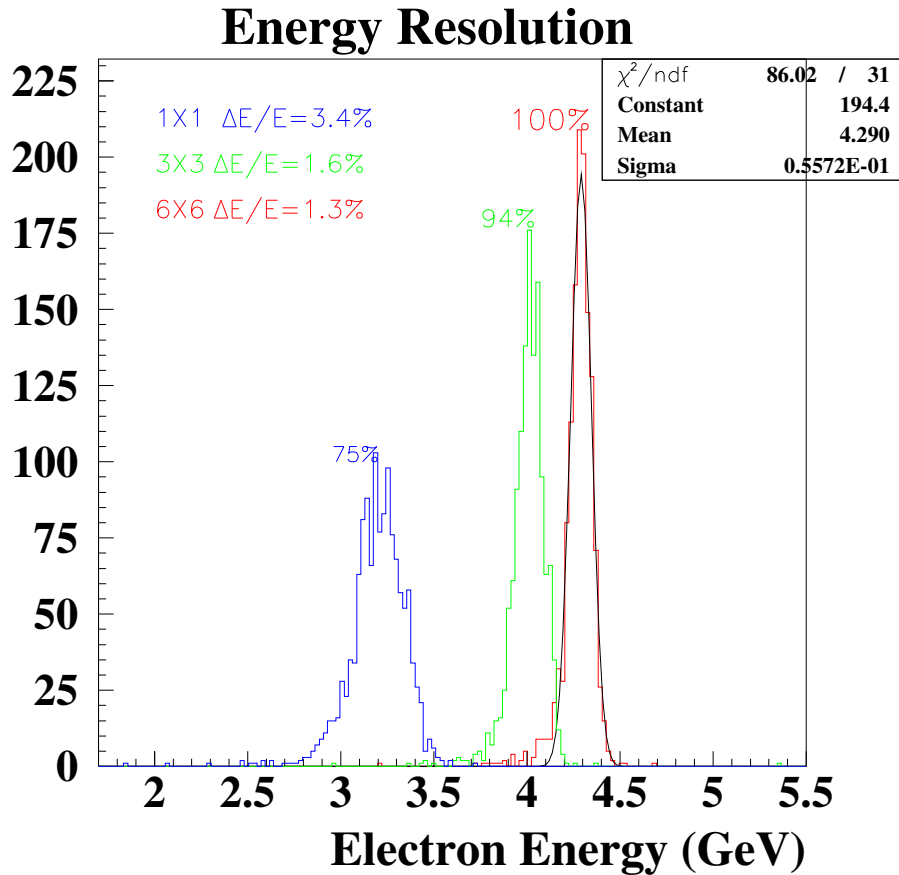
Energy Resolution

1X1 ΔE/E=3.4%

3X3 ΔE/E=1.6%

6X6 ΔE/E=1.3%

χ^2/ndf	86.02 / 31
Constant	194.4
Mean	4.290
Sigma	0.5572E-01

75%   94%   100%

Electron Energy (GeV)

Figure 18: Energy response of a $PbWO_4$ crystal array to 4.3 GeV electrons. Left peak: single crystal; center peak: 3×3 array; right peak: 6×6 array.

tions is shown in Figure 23. As is well known, there is a rather strong correlation between the position resolution (σ_x) and the point at which the incoming electrons or photons hit the detector face. The bottom plot of the figure shows this dependence for the $PbWO_4$ crystals. The σ_x is smaller (1.28 mm) near the edge of the cell and increases to 2.1 mm at the cell center.

Similar to the energy reconstruction, one can expect degradation in the position resolution in the transition region as the photon beam passes from the last lead tungstate crystal module to the lead glass region. This dependence is shown in Figure 24. Though the simple center-of-gravity reconstruction exhibits typical oscillation of reconstructed *versus* impact position with a relatively larger amplitude, the corrected logarithmic method shows a good linear transition from lead tungstate to lead glass regions.

Good position and energy resolutions achieved for the HYCAL calorimeter provided critical improvements in both two gamma invariant mass and production angle reconstructions. As an example, in Figure 25 is shown the two gamma invariant mass distribution extracted
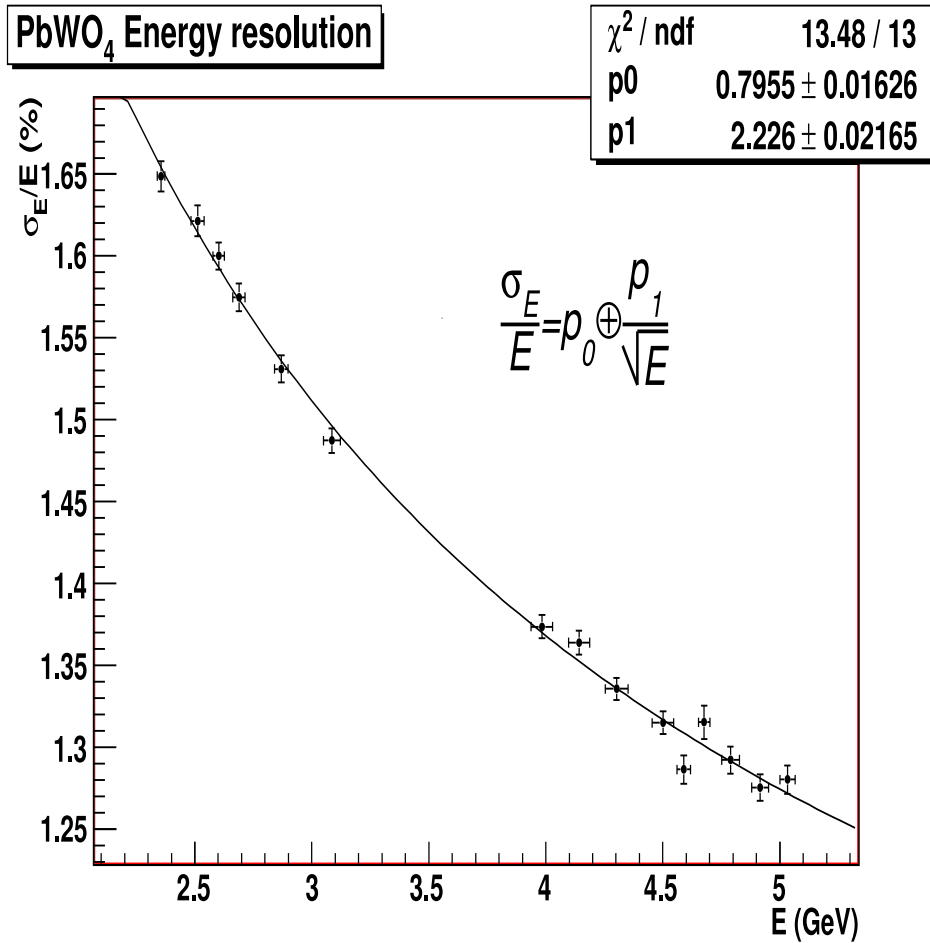
Figure 19: Measured energy resolution *versus* photon beam energy for the $PbWO_4$ part of the calorimeter.

from PrimEx I experimental data set collected in 2004. An excellent resolution of $\sigma_{\gamma\gamma} = 2.3$ MeV provided precision extraction of events over the experimental background.

5.5.4 HYCAL Gain Monitoring System

To control the stability of gains for each channel of the calorimeter during the long data taking periods, a gain monitoring system was developed and constructed. This system is based on feeding light pulses from a central LED based light source distributed by fiber optics cables to the front part of each module. The main components of the Light Monitoring System (LMS) are: (1) a light source, (2) a mixing box, (3) a light distribution system, (4) filter wheel, (5) reference detectors and (5) a dedicated data acquisition system. The optical components and the reference detectors are mounted in a thermally insulated box whose temperature is controlled at a level of 0.1°C.

Long term stability tests of the prototype LMS system, as well as several beam tests, have
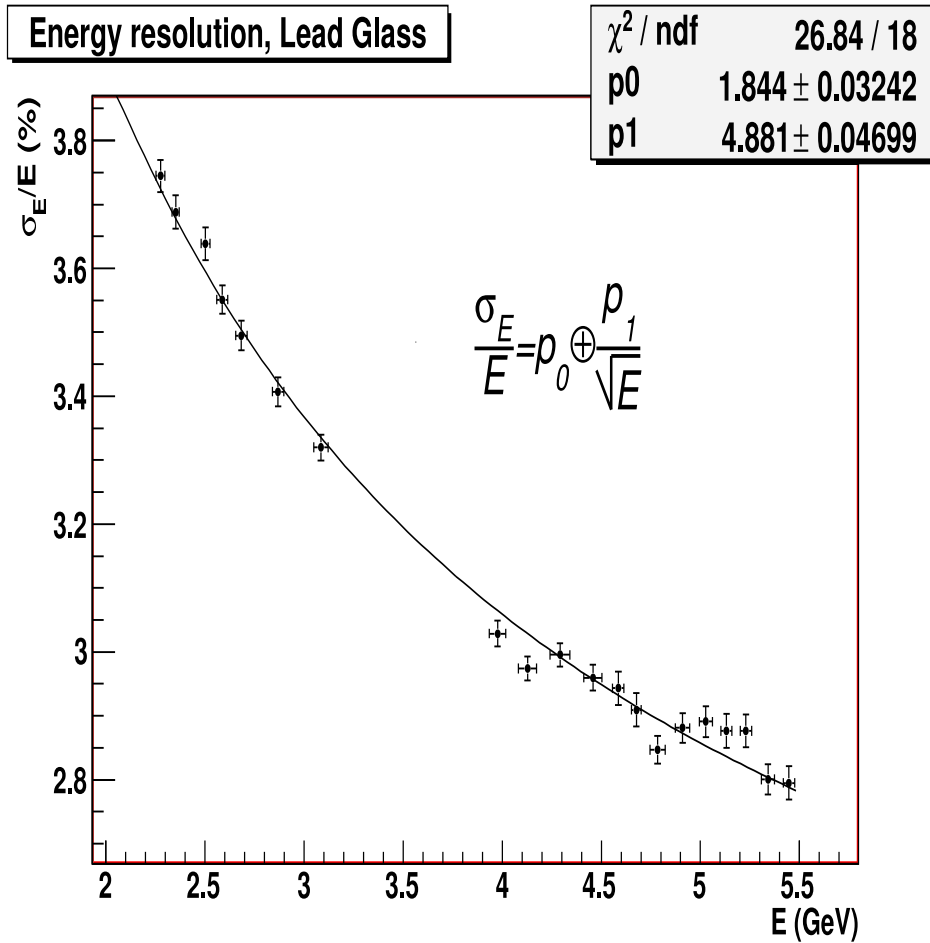
Figure 20: Measured energy resolution *versus* photon beam energy for the lead glass part of the calorimeter.

been performed. For this tests, the light intensity was monitored with a PIN photodiode and three reference PMTs. In figure 26, top picture, the distribution of the ratio, PMT_1/PMT_3, for a period of 540 hours is shown. The same ratio plotted *versus* time is presented in the bottom picture.

During the data taking period in 2004 it was observed that the LMS reference detectors are somewhat sensitive to the change of magnetic field from the nearby pair spectrometer dipole. This change of signals was observed at the level of 1.5% on the reference PMT signals. We plan to fix this problem by adding more magnetic insulation and/or trying to replace the PMTs on the reference detectors with less sensitive photodetectors for the *PrimEx II* run in Hall B.

This existing device will provide a high resolution and large acceptance calorimeter for the proposed η decay width measurement in Hall D.
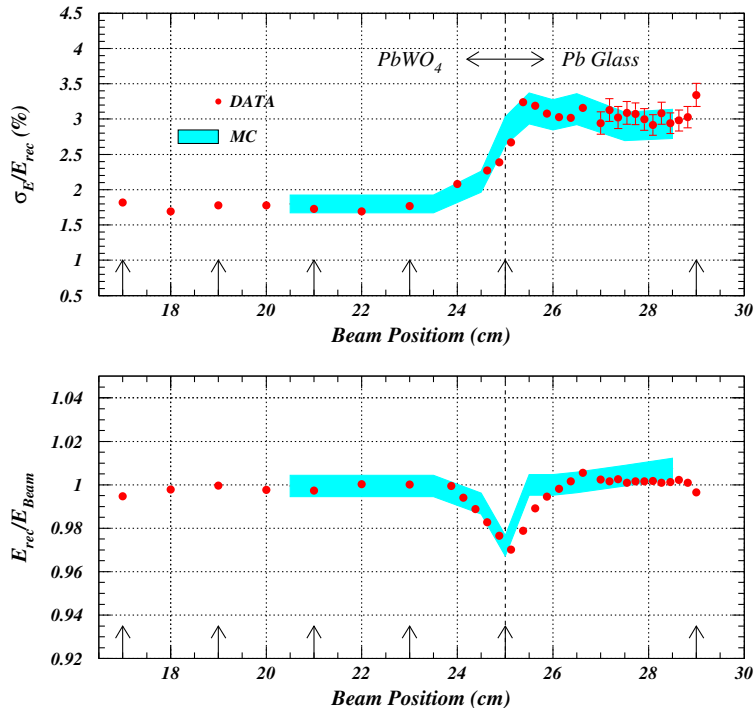
Figure 21: Beam test results for the transition region between $PbWO_4$ and lead glass modules. Top: energy resolution. Bottom: relative reconstructed energy *versus* position. The gray bands indicate Monte Carlo simulations.

6 Geometrical Acceptance and Experimental Resolutions

To achieve a high precision on the η lifetime measurement, the geometrical acceptance and experimental resolutions are two important concerns for design of the experiment. In order to optimize the experiment design, we have investigated several issues: target thickness, collimator size, and the distance between target and calorimeter. We also explored different options of the calorimeter: FCAL, existing HYCAL hybrid calorimeter, and upgraded HYCAL. As discussed below, the HYCAL calorimeter provides significant advantages in experimental resolutions as compared to the FCAL calorimeter. Resolutions in energy, production angle, and the invariant mass of the two decay photons are critical for the high precision extraction of the forward eta photoproduction cross section from this high background experimental environment. We plan to use three major systems for this experiment: (1) the photon tagging facility, with the photon collimation system and the pair spectrometer; (2) the liquid targets; (3) and the HYCAL hybrid electromagnetic calorimeter. It will provide sufficient geometrical acceptance and experimental resolutions with a minimum cost. We are also considering upgrading our existing HYCAL calorimeter, replacing the rest of

Position Resolution

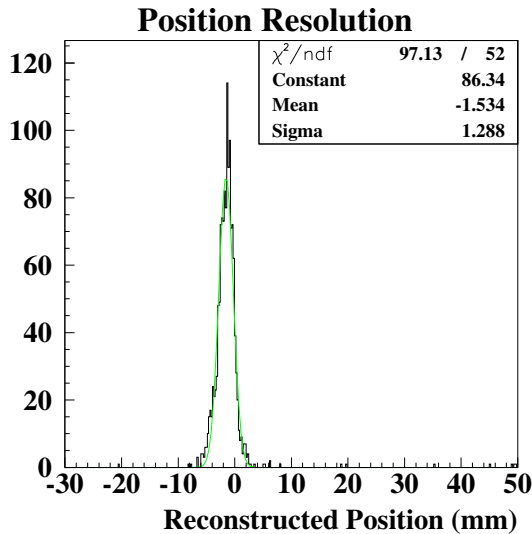|	
χ^2/ndf	97.13 / 52
Constant	86.34
Mean	-1.534
Sigma	1.288

Reconstructed Position (mm)

Figure 22: Distribution of reconstructed positions at the boundary between two lead tungstate crystal detectors.

the lead glass modules with crystal detectors. That will be 118×118 cm^2 in size and will possibly serve as a moderate acceptance, high resolution and radiation hard calorimeter to be used in other high precision experiments at JLab. The detail of this study is described as below.

6.1 Geometrical Acceptance

Figure 27 shows the geometrical acceptance of the η events produced at forward angles ($\theta_\eta = 0.05°$) by HYCAL as a function of the target to calorimeter distance. Figure 28 shows the geometrical acceptance of the HYCAL as a function of the η production angles. As it can be seen, the relatively large size of the HYCAL calorimeter provides good 60% coverage of the events for the target to calorimeter distance of about 6.5 meters. Similar calculations for the GlueX standard FCAL yield about 75% geometrical efficiency at similar distances, which is a consequence of the larger size of the FCAL calorimeter. In this experiment, we are interested in forward eta production. Both HYCAL and FCAL can provide enough geometrical acceptance.

6.2 Experimental Resolutions

Resolution in θ_η is of particular importance in the identification of the forward peaked η's photoproduced by the Primakoff mechanism ($\theta_\eta \sim 0.2°$) from η's produced at larger angles via the nuclear field. The η production angle can be determined from the measured photon energies and angles by:
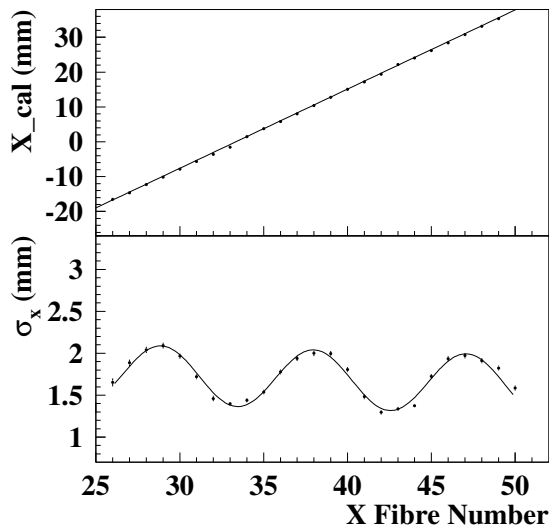
Figure 23: Reconstructed *versus* actual position (top) and position resolution (bottom) across the face of $PbWO_4$ crystal array.

$$cos\theta_\eta = \frac{E_{\gamma 1}cos\theta_{\gamma 1} + E_{\gamma 2}cos\theta_{\gamma 2}}{\sqrt{E_{\gamma 1}^2 + E_{\gamma 2}^2 + 2E_{\gamma 1}E_{\gamma 2}cos\psi_{\gamma 1\gamma 2}}}. \tag{9}$$

For the determination of the photon angles, the interaction vertex of the reaction in the target is required. Unfortunately, in this experiment we can not detect the recoil nuclei because of their very small energies. Therefore, the beam spot size at the target could be potential limiting factor of the θ_η resolution. The size of the beam spot is directly associated to the size of primary collimator in the beam line. For illustration, figure 29 shows the x and y-distribution of events on the target used in these simulations for the $R = 2mm$ beam collimator. Figure 30 shows the calculated angular resolution as a function of the photon beam collimator radius, and figure 31 shows the projected angular resolutions for three different calorimeters: FCAL, HYCAL, and upgraded HYCAL. As it can be seen, the HYCAL calorimeter with its $70 \times 70cm^2$ high resolution $PbWO_4$ insertion provides a factor of two better angular resolution than the FCAL calorimeter. For proposed HYCAL, the resolution in the production angle is still reasonably small up to a collimator radius of $R = 2.5$ mm.

Another important event selection criteria in this experiment is the invariant mass of two photons detected in the calorimeter. As can be seen from figure 32, the HYCAL calorimeter will provide a factor of two better invariant mass resolution than the FCAL all lead glass calorimeter.

By similar arguments, the unknown z-position of the interaction vertex in the target will contribute to the experimental resolutions of the reconstructed production angle and two photon invariant mass. Figure 33 shows the expected θ_η resolution for different target
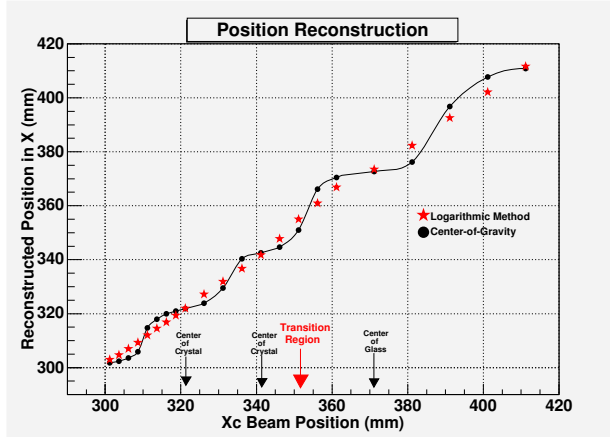
34

Figure 24: Reconstructed *versus* impact coordinate at the transition region of the HYCAL calorimeter.

lengths, simulated for a fixed beam collimator size of $R = 2mm$ and for a target to calorimeter distance of $6.5m$. As it is clearly seen, the $30cm$ cryogenic targets planned for the GlueX setup can be used in the proposed experiment. We have also done similar simulations for the invariant mass, and do not see any significant degradation in the resolution *versus* target length.

One interesting approach could be to try to increase the target to FCAL calorimeter distance in order to improve the resolutions in θ_η production angle and in invariant mass. We have done simulations moving the FCAL calorimeter from 6 to 12 m (reasonable dimensions of Hall D), and the results are shown in Figure 34. The lack of any sizable improvement in resolutions, demonstrates once more that the experimental resolutions in both production angle and invariant mass are dominated by energy resolution at these forward production angles. As such, the only improvement in the resolutions may come from the HYCAL hybrid calorimeter, which we are suggesting to be used in this proposed experiment. Further, a highly segmented and all $PbWO_4$ updated HYCAL would provide the best resolutions in the experiment.

7 Calibration of the Systematic Error with Compton Scattering

The key to the proposed experiment is the measurement of the absolute cross section of η photoproduction at small forward angles. The invariant mass and the production angle of the η's will be reconstructed by detecting the two decay photons from the $\eta \to \gamma\gamma$ reaction in the HYCAL calorimeter. It is crucial to calibrate the overall systematic errors of the experimental setup by well known physics processes with similar kinematics in the identical experimental configuration.

The proposed experimental setup provides a unique opportunity to verify the luminosity normalization procedure (including both photon flux and target thickness) and to monitor
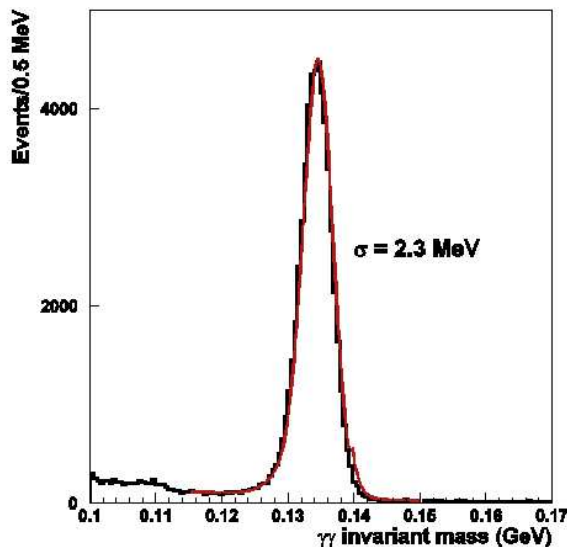
Figure 25: Reconstructed two gamma invariant mass from the *PrimEx I* data set.

the stability of the experiment by measuring the absolute cross section for a well known electromagnetic process, namely Compton scattering from atomic electrons, simultaneously during the η production run. It provides a comprehensive check of the overall setup, as its kinematics are in many ways similar to those involved in detecting the η via $\eta \to \gamma\gamma$, see figure 35.

The scattering of photons by free electrons $\gamma + e \to \gamma' + e'$ is one of the simplest and most basic quantum-electrodynamic processes that is experimentally accessible. The lowest order Compton scattering diagrams were first calculated by Klein and Nishina in 1929 [25], and by Tamm in 1930 [26]. There are two types of corrections to the basic Klein-Nishina formula which must be considered when studying Compton scattering at energies above 0.1 GeV. These are radiative corrections, and double Compton scattering contributions. The interference between the basic first order single Compton scattering amplitude and the radiative and double Compton scattering amplitudes have been discussed extensively in the literature [27]-[29], [30],[31], and the errors on the theoretical calculations are less than 1%. The total Compton cross section and the forward scattering cross section with radiative and double Compton corrections have been calculated with different numerical methods[33][34]. In the case of the total cross section they are also compared to the National Institute of Standards and Technology (*NIST*) values. They are in good agreement, namely, within 0.5%. As such, Compton scattering provides an excellent means to control the systematic errors of the *PrimEx* experiment, including the photon flux, target thickness, and the HYCAL calorimeter detection efficiency.

During our experiment on π^0 lifetime measurement in 2004, the Compton scattering data set was collected on a 5% radiation length ^{12}C target with incident photon beam energies of 4.85 - 5.45 GeV. From the extracted yield, combined with luminosity and detector acceptance
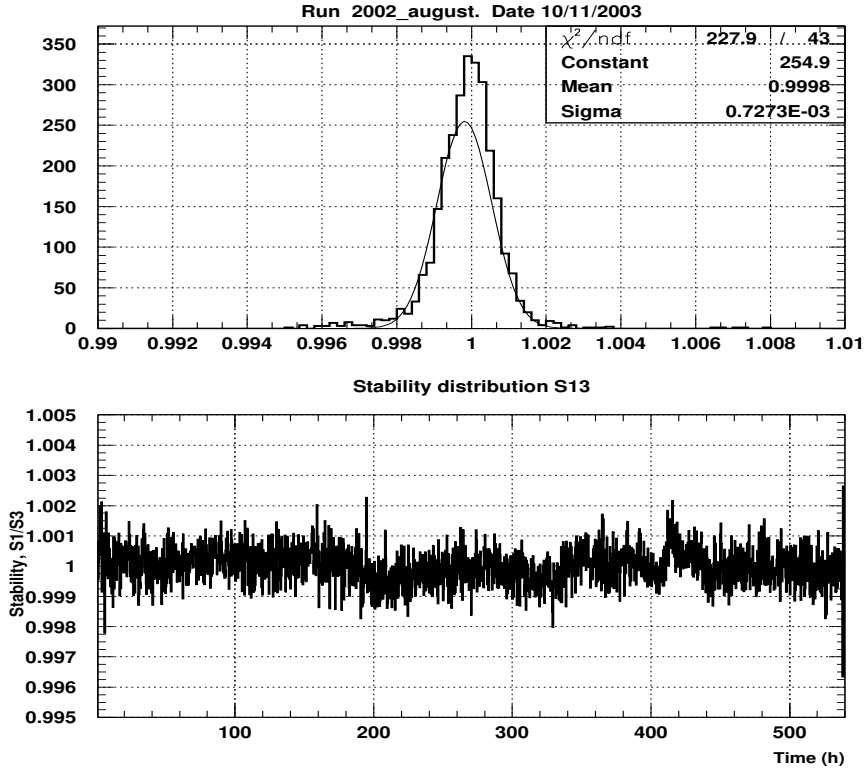
Figure 26: Stability of the light monitoring system.

information, the preliminary results for the differential cross section in the forward direction over the HYCAL acceptance were obtained, as shown in Figures 36. These data are in excellent agreement with theory predictions with a 14% confidence level. For each data point with an energy resolution of 2% defined by two T-counters of the Hall B tagger, an average systematic error of 1.28%, a statistical error of 0.59%, and an average total error of 1.41% have been obtained. The time stability of the Compton cross section measurement was also performed and a 2% stability during the entire *PrimEx* running period (3 months) was achieved. This demonstrates that the absolute cross section measurement on Compton scattering provides an excellent tool to calibrate and monitor the *PrimEx* systematical errors.

In this experiment, we plan to take Compton data in parallel with the η production runs. For photon energies from 10.5 GeV to 11.7 GeV, the HYCAL calorimeter must be located at least ~ 6.5 m from the target in order to have acceptance for the Compton events. Monte Carlo simulations indicate that we will be able to detect the photon-electron pairs from Compton scattering in the forward direction at $\theta_\gamma \sim 0.55°$ (see figure 37). The Compton production rates are 28.9 Hz for LH_2, 25.3 Hz for $LHe4$, and 14.4 Hz for ^{12}C targets. These will provide enough statistics to measure the absolute Compton scattering cross section at $\theta_\gamma \sim 0.55°$ in the 10.5 GeV to 11.7 GeV energy range at the $\sim 1\%$ level.
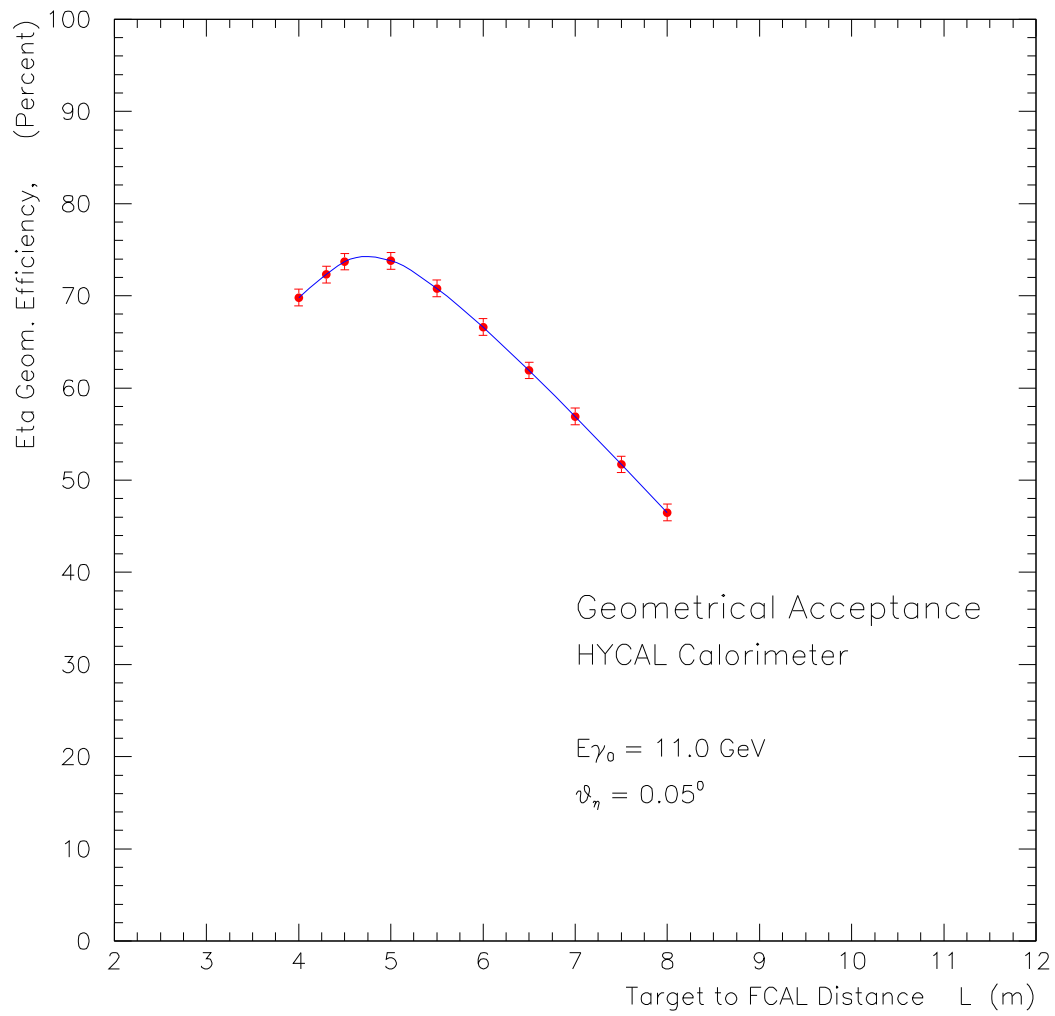
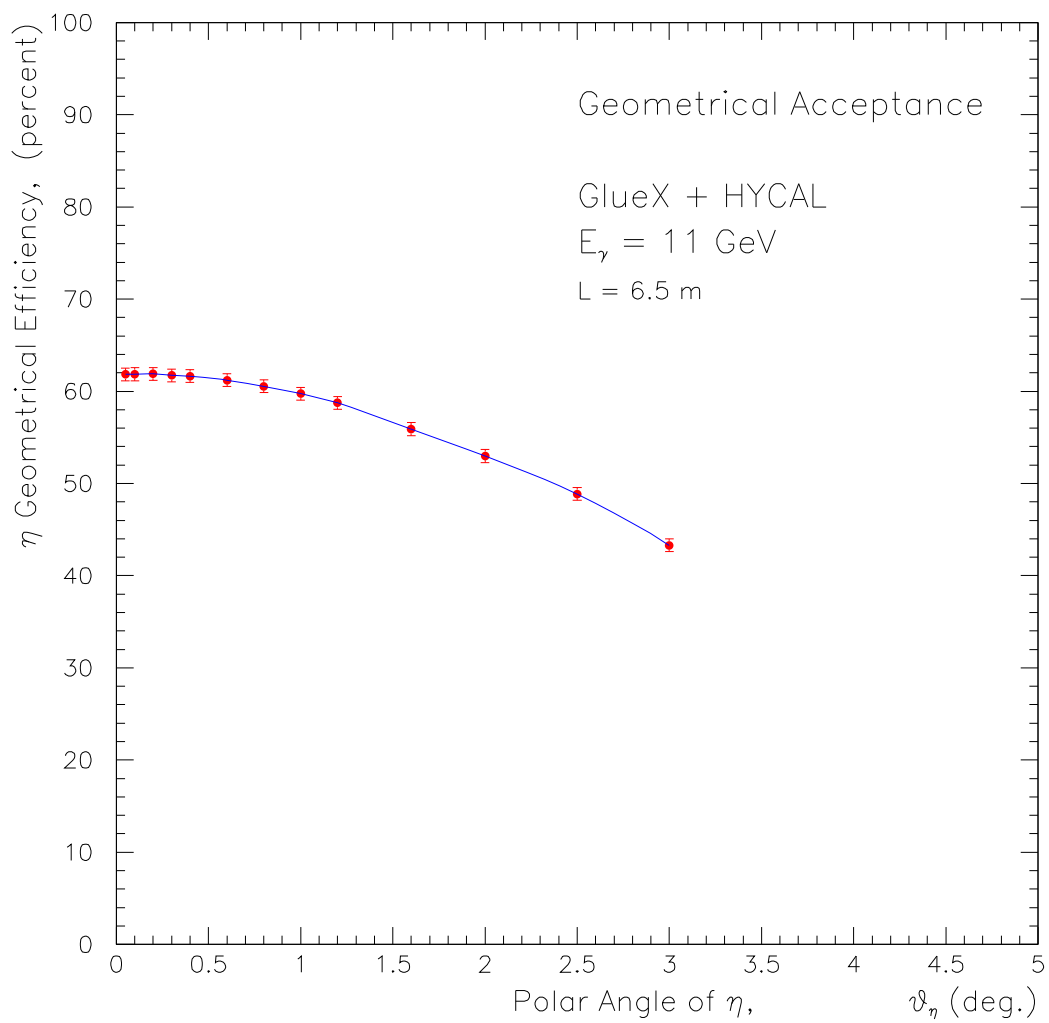Figure 27: Geometrical acceptance of the HYCAL calorimeter *versus* target to calorimeter distance.

Figure 28: Geometrical acceptance of HYCAL calorimeter *versus* η production angle.

8   Theoretical Study of η Forward Photoproduction off Complex Nuclei

The coherent photoproduction of the η in a nucleus:

$$\gamma + A \rightarrow \eta + A \tag{10}$$

can be described by the sum of Coulomb T_C and Strong T_S amplitudes. Including incoherent production, the differential cross section is:

$$\frac{d\sigma}{d\Omega} = \frac{k^2}{\pi}\frac{d\sigma}{dt} = \mid T_C + e^{i\varphi}T_S \mid^2 + \frac{d\sigma_{inc}}{d\Omega} \tag{11}$$

where $\frac{d\sigma_{inc}}{d\Omega}$ is the incoherent cross section *i.e.* processes involving target nucleus excitation or break up. Each of these amplitudes factorizes into a photoproduction amplitude on a nucleon multiplied by a corresponding form factor. In addition, these form factors must be modified for the final state interactions of the outgoing mesons with nucleons. Interaction of incident photons with the nuclear matter give rise to the shadowing effect which must be considered as well.

In order to extract the η radiative decay width from the *PrimEx* data with high precision, the shapes of each term in equation (11) need be understood theoretically as accurately as possible. Below, we present the results of our extensive studies of this subject.

8.1   Photoproduction in the Coulomb field of nuclei

The effect of the meson Final State Interactions in nuclei (FSI) had been first discussed in detail by G. Morpurgo [35], who considered absorption of the produced mesons in the strong field of nuclei using the Distorted Wave Approximation (DWA). Calculations of the electromagnetic and strong form factors in this work have been done with a uniform nuclear density distribution $\rho(r)$. Based on these two assumptions, part of the correction to the strong and electromagnetic form factors, which takes into account meson absorption in nuclei, is correctly obtained. However, the effect of the meson re-scattering to forward angles was not taken into account in this work. This effect is important for the precision extraction of the decay widths since mesons initially produced at modest angles can re-scatter to small angles. This effect was first considered by G.Fäldt [36] in non-diffractive production processes on nuclei in the framework of the Glauber theory of multiple scattering [37]. A general expression (eq. 3.2 in [36]) is obtained here, but an analytically integral formula is derived for the case of equal absorption between the incident and produced particles only (eq. 3.4), which is not the case for the photoproduction processes.

8.1.1 The electromagnetic form factor

In the past several years, we developed a model [38, 39] based on Glauber theory of multiple scattering, using the independent particle model for nucleons, and taking into account the FSI of mesons in nuclei and Fäldt's rescattering effect. The Coulomb amplitude of the photoproduction of mesons on nuclei can be expressed as:

$$T_C = Z\sqrt{8\alpha\Gamma}(\frac{\beta}{m_\pi})^{3/2}\frac{k^2 sin\theta}{q^2 + \Delta^2}F_{em}(q, \Delta) \tag{12}$$

where the electromagnetic form factor is given by [38]:

$$F_{em}(q, \Delta) = \frac{q^2 + \Delta^2}{q}\int J_1(qb)\frac{bd^2bdz}{(b^2 + z^2)^{3/2}}e^{i\Delta z}$$
$$\times \exp\left(-\frac{\sigma\prime}{2}\int_z^\infty \rho(b, z\prime)dz\prime\right)\int_0^{\sqrt{b^2+z^2}} x^2\rho(x)dx \tag{13}$$

with the following notation:

$$\sigma\prime = \sigma\left(1 - i\frac{Ref(0)}{Imf(0)}\right) = \frac{4\pi}{ik}f(0) \tag{14}$$

Where σ is the ηN total cross section, f(0) is the $\eta N \to \eta N$ forward amplitude. The invariant transfer momenta is expressed through the two dimensional transverse momenta $q = |\vec{q}|$ and longitudinal momenta Δ:

$$t = -q^2 - \Delta^2 = -4kpsin^2(\frac{\theta}{2}) - (\frac{m_\pi^2}{2k})^2$$

where $k = |\vec{k}|$ and $p = |\vec{p}|$ are the photon and η momenta.

In equation (14), $\rho(r)$ is the nuclear density, $J_1(x)$ is the first order Bessel function [40]. The integration in (14) goes over impact parameter b, which is the two-dimensional vector in the plane perpendicular to direction of motion and longitudinal coordinate z. Here the Coulomb form factor $F_{em}(q, \Delta)$ acquires an imaginary part due to the longitudinal momentum transfer Δ and the presence of the real part of the ηN elastic forward amplitude in the absorption process.

The main properties of the Coulomb production are: it rises from zero at zero angle; reaching its maximum at $q = \Delta = \frac{m_\pi^2}{2k}$ with the specific energy dependence $\frac{d\sigma}{dt} \sim k^2$. These properties allow one to separate the Coulomb production (Primakoff process) from the competing nuclear production in strong field of nuclei which is peaks at relatively large production angles.

8.1.2 Effect of light nuclei

The photoproduction of mesons in the electromagnetic field of light nuclei requires special consideration. The expression (14) was obtained in the optical limit which works better

(is valid) for extended nuclear matter (heavy nuclei). For the light nuclei we obtain the electromagnetic form factor based on the multiple scattering theory [37, 36]:

$$
\begin{aligned}
F_{em}(q) &= 2\pi \frac{q^2 + \Delta^2}{q} \int J_1(qb) \frac{b^2 db dz}{(b^2 + z^2)^{3/2}} e^{i\Delta z} (1 - G(b, z))^{A-1} \\
&\times \int_0^{\sqrt{b^2 + z^2}} x^2 \rho_{ch}(x) dx \\
G(b, z) &= \frac{f_s(0)}{ika_s} \int_z e^{-\frac{(\vec{b} - \vec{s}')^2}{2a_s}} \rho(s', z') d^2 s' dz' \\
&= \frac{\sigma'}{2a_s} \int_z e^{-\frac{b^2 + s'^2}{2a_s}} I_0(\frac{bs'}{a_s}) \rho(s', z') s' ds' dz'
\end{aligned}
\tag{15}
$$

$$
\begin{aligned}
F_{em}(q) &= 2\pi \frac{q^2 + \Delta^2}{q} \int J_1(qb) \frac{b^2 db dz}{(b^2 + z^2)^{3/2}} e^{i\Delta z} (1 - G(b, z))^{A-1} \\
&\times \int_0^{\sqrt{b^2 + z^2}} x^2 \rho_{ch}(x) dx \\
G(b, z) &= \frac{f_s(0)}{ika_s} \int_z e^{-\frac{(\vec{b} - \vec{s}')^2}{2a_s}} \rho(s', z') d^2 s' dz' \\
&= \frac{\sigma'}{2a_s} \int_z e^{-\frac{b^2 + s'^2}{2a_s}} I_0(\frac{bs'}{a_s}) \rho(s', z') s' ds' dz'
\end{aligned}
\tag{16}
$$

Here $I_0(x)$ is the zero order Bessel function of imaginary argument [40]). In deriving this expression, the commonly used parametrization [41] for the elastic $\eta N \to \eta N$ amplitude $f_s(q) = f_s(0) exp(-a_s q^2 / 2)$ has been adopted.

For the light nuclei, such as carbon, the nuclear density function $\rho(r)$ corresponding to the harmonic oscillator potential well is widely accepted (used) in the literature [42]:

$$
\rho(r) = \frac{4}{\pi^{3/2} a_0^3 A} (1 + \frac{A - 4}{6 a_0^2} r^2) e^{-\frac{r^2}{a_0^2}}
\tag{17}
$$

The charge distribution $\rho_{ch}(r)$ in the nuclei is obtained by convolution of the nuclear density with the proton's charge distribution. For the latest we adopt the Gaussian parametrization: $\rho_p(r) = \frac{1}{\pi^{3/2} r_p^3} e^{-\frac{r^2}{r_p^2}}$. With that, the nuclear charge density can be expressed by:

$$
\begin{aligned}
\rho_{ch}(r) &= \int d^3 r \prime \rho(r\prime) \rho_p(|\vec{r} - \vec{r}\prime|) \\
&= \frac{4}{\pi^{3/2} A(a_0^2 + r_p^2)^{3/2}} \left(1 + \frac{(A - 4)}{6} [\frac{3 r_p^2}{2(a_0^2 + r_p^2)} + \frac{a_0^2 r^2}{(a_0^2 + r_p^2)^2}] \right) e^{-\frac{r^2}{r_p^2 + a_0^2}}
\end{aligned}
\tag{18}
$$

For illustration, Figure 38 and 39 show the angular behavior of Coulomb form factors calculated by expression (16)(18) for helium and carbon nuclei with 11 GeV incident photon beam. In this calculation the nuclear density $\rho(r)$ was parametrized by Fourie-Bessel analysis from the recent electron scattering data [43, 44]. As it can be seen, the final state interaction effects are more emphasized at larger angles and are small at the forward Primakoff region.

8.1.3 Nuclear excitation by Coulomb exchange

In addition to the coherent photoproduction in the Coulomb field, production of the η with a nuclear collective excitation (for instance, the giant dipole resonance) is also possible. Such processes first discussed in [46], where for the inelastic form factor the following approximation had been obtained:

$$|F_n(q)|^2 \approx \frac{1.4N}{2m_p ZAE_{av}}|t| \tag{19}$$

where m_p and E_{av} are the proton mass and the average excitation energy of the nucleus having Z protons and N neutrons. The longitudinal momentum transfer in the case of η photoproduction with nuclear collective excitation is much larger than in the coherent photoproduction: $\Delta_{in} = \Delta + E_{av} \gg \Delta$. Using that fact the ratio of the "elastic" to the "inelastic" cross sections of the η photoproduction in the Coulomb field, one can estimate:

$$R = \frac{\frac{d\sigma_{in}}{d\Omega}}{\frac{d\sigma_{el}}{d\Omega}} \approx \frac{(q^2 + \Delta^2)^2}{(q^2 + \Delta_{in}^2)^2}\frac{|F_n(q)|^2}{|F(q)|^2} \approx \frac{1.4N}{2m_p ZAE_{av}}\frac{(q^2 + \Delta^2)^2}{(q^2 + \Delta_{in}^2)} \tag{20}$$

For the carbon nucleus the average collective excitation energy is on the level of $E_{av} \approx 20 - 25 MeV$ which using the formula (9) leads to the $R \approx 10^{-7}$ at the Coulomb peak region ($q = \Delta = \frac{m_\eta^2}{2k}$). Thus the contribution from the nuclear collective excitations can be safely neglected for the GeV and more incident photon energies .

8.2 Coherent photoproduction in the strong field of nuclei

8.2.1 Strong Amplitude T_s

The main impact on the lifetime extraction from the measured differential cross sections comes comes from our knowledge of the strong amplitude T_S in the coherent process of the reaction:

$$\gamma + A \rightarrow \eta + A \tag{21}$$

In Glauber theory of multiple scattering [47] this coherent photoproduction amplitude is given by:

$$
\begin{aligned}
T_S(q, \Delta) &= A\frac{ik}{2\pi}\int e^{i\vec{q}\cdot\vec{b}+i\Delta z}\Gamma_p(\vec{b} - \vec{s})\rho(\vec{s}, z) \\
&\times \ [1 - \int \Gamma_s(\vec{b} - \vec{s}\prime)\rho(\vec{s}\prime, z\prime)d^2 s\prime dz\prime]^{A-1}d^2 b d^2 s dz
\end{aligned} \tag{22}
$$

The two dimensional vectors $\vec{b}$ and $\vec{s}$ are the impact parameter and the nucleon coordinate in the plane transverse to the incident photon momenta; z is the longitudinal coordinate of the nucleon in the nucleus. The profile functions $\Gamma_{p,s}(\vec{b} - \vec{s})$ are the two dimensional

Fourier transformation of elementary amplitudes for the eta photoproduction off the nucleon $f_p = f(\gamma + N \rightarrow \eta + N)$ and elastic pion-nucleon scattering $f_s = f(\eta + N \rightarrow \eta + N)$:

$$\Gamma_{p,s}(\vec{b} - \vec{s}) = \frac{1}{2\pi i k} \int e^{i\vec{q}\cdot(\vec{b}-\vec{s})} f_{p,s}(q) d^2q \tag{23}$$

We parameterized the elementary production amplitudes in the standard way:

$$\begin{aligned}
f_p &= \phi(0)(\vec{h} \cdot \vec{q}) e^{-\frac{a_p q^2}{2}} \\
f_s &= f_s(0) e^{-\frac{a_s q^2}{2}}
\end{aligned} \tag{24}$$

Here $\phi(0)$, $f_s(0)$ and a_p, a_s are the forward elementary amplitudes and their relevant slopes. $\vec{h} = [\vec{k} \times \vec{\epsilon}]$ The relevant profile functions:

$$\begin{aligned}
\Gamma_p(\vec{b} - \vec{s}) &= \frac{\vec{h} \cdot (\vec{b} - \vec{s})}{k a_p^2} \phi(0) e^{-\frac{(\vec{b}-\vec{s})^2}{2a_p}} \\
\Gamma_s(\vec{b} - \vec{s}) &= \frac{f_s(0)}{ik a_s} e^{-\frac{(\vec{b}-\vec{s})^2}{2a_s}}
\end{aligned} \tag{25}$$

Substituting expressions in (22) we obtain:

$$\begin{aligned}
T_S(q, q_L) &= A(\vec{h} \cdot \vec{q})\phi(0) F_S(q, q_L) \\
F_S(q, q_L) &= \frac{2\pi}{q a_p^2} \int J_1(qb)(b I_0(\frac{bs}{a_p}) \\
&\quad - s I_1(\frac{bs}{a_p})) e^{i\Delta z} e^{-\frac{b^2+s^2}{2a_p}} \rho(s, z)(1 - G(b, z))^{A-1} b\,db\,ds\,dz \\
G(b, z) &= \frac{f_s(0)}{ik a_s} \int_z e^{-\frac{(\vec{b}-\vec{s}')^2}{2a_s}} \rho(s', z') d^2s' dz' \\
&= \frac{\sigma'}{2a_s} \int_z e^{-\frac{b^2+s'^2}{2a_s}} I_0(\frac{bs'}{a_s})\rho(s', z') s'\,ds'\,dz'
\end{aligned} \tag{26}$$

Here I_0, I_1 are the zero and first order Bessel functions of imaginary arguments. Figure 40 and 41 show the strong form factor square with and without final state interaction corrections for ^{4}He and ^{12}C targets.

8.3   Photon shadowing in nuclei

Real photons at high energy are shadowed in nuclei [41]. The photon shadowing in η photoproduction is a result of two step processes [45]: the initial photon produces a vector meson in the nucleus, which consequently produces an η meson after multiple scattering. The main contribution to such two step photoproduction comes from the ρ mesons, as the cross section for ρ photoproduction from the nucleon is almost in order of magnitude higher than for the

ω production.

The amplitude relevant to two step process $\gamma \rightarrow \rho \rightarrow \eta$ in multiple scattering theory is given by:

$$
\begin{aligned}
T_I(q) &= \frac{ik}{2\pi} A(A-1) \int e^{i\vec{q}\cdot\vec{b}} d^2 b \Gamma_p(\vec{b}-\vec{s}_1) \Gamma_s(\vec{b}-\vec{s}_2) \rho(s_1, z_1) \rho(s_2, z_2) \\
&\times \quad \theta(z_2 - z_1) e^{i\Delta_\rho(z_1-z_2)+i\Delta z_2} (1 - G(b, z_1))^{A-2} d^2 s_1 d^2 s_2 dz_1 dz_2 \\
G_s(b, z_1) &= \int_{z_1}^{\infty} \Gamma_s(\vec{b}-\vec{s'}) \rho(s', z') d^2 s' dz
\end{aligned} \tag{27}
$$

where $\Delta_\rho = \frac{m_\rho^2}{2E}$ is the longitudinal momentum transfer in the elementary reaction $\rho + N \rightarrow \eta + N$. Using equations (25) this expression can be expressed in the form convenient for the numerical integration [38]

$$
\begin{aligned}
T_I(q) &= A(\vec{h}\cdot\vec{q}) f_p(0) F_{SI} \\
F_{SI} &= (A-1) \frac{\pi\sigma'}{q a_s a_p^2} \int J_1(qb) I_0\left(\frac{bs_2}{a_s}\right) \left[b I_0\left(\frac{bs_1}{a_p}\right) - s_1 I_1\left(\frac{bs_1}{a_p}\right) \right] \\
&\times \quad \theta(z_2 - z_1) \rho(s_1, z_1) \rho(s_2, z_2) e^{-\frac{(a_p+a_s)b^2}{2a_p a_s}} e^{-\frac{s_1^2}{2a_p} - \frac{s_2^2}{2a_s}} e^{i\Delta_\rho(z_1-z_2)+i\Delta z_2} \\
&\times \quad (1 - G(b, z_1))^{A-2} b \, db \, s_1 \, ds_1 \, s_2 \, ds_2 \, dz_1 \, dz_2
\end{aligned} \tag{28}
$$

The complete strong amplitude accounting for the photon shadowing reads:

$$
\begin{aligned}
T_S(q) &= A(\vec{h}\cdot\vec{q}) \phi(0) [F_S - w F_I] \\
w &= \frac{f(\gamma N \rightarrow \rho N) f(\rho N \rightarrow \pi N)}{f(\rho N \rightarrow \rho N) f(\gamma N \rightarrow \pi N)}
\end{aligned} \tag{29}
$$

where the range of the shadowing parameter w is between zero (no shadowing) and one (Vector dominance model).

Figure 42 shows the square of the strong form factor for carbon calculated with different photon shadowing parameters, where the shadowing parameter $w = 0.25$ is in accordance with the experimental data [48, 49]. The oscillator type of nuclear density (17) is used in the calculations.

9   Incoherent photoproduction

Incoherent pion photoproduction is a production with the excitation or breakup of the target nuclei:

$$
\gamma + A \rightarrow \eta + A' \tag{30}
$$

The general expression for the incoherent cross section established in the literature [50, 51] is given by:

$$
\frac{d\sigma_{inc}}{d\Omega} = \frac{d\sigma_0}{d\Omega}(q) N(0, \sigma)(1 - G(t)) \tag{31}
$$

where $\frac{d\sigma_p}{d\Omega}$ is the elementary cross section on nucleon $\gamma + N \to \eta + N$, and

$$N(0, \sigma) = \int \frac{1 - e^{-\sigma T(b)}}{\sigma} d^2 b \tag{32}$$

Here $T(b) = A \int \rho(b, z) dz$; The factor $(1 - G(t))$ takes into account the suppression of η mesons produced at small angles due to Pauli exclusion principle [50]. For the light nuclei (like carbon) this factor can be expressed as

$$G(t) = [1 + (\frac{q^2 R^2}{15})^2] e^{-\frac{2q^2 R^2}{15}} \tag{33}$$

The factorization in (31) is valid only for the Born approximation (without meson absorption). As was shown in the case of the proton elastic scattering on nuclei [52], the consideration of the absorption process in the final state changes substantially this expression.

Assuming that the photoproduction cross section on the nucleon is completely determined by the single-flip process in the elementary amplitude:

$$\frac{d\sigma_p}{d\Omega} = c_p q^2 e^{-a_p q^2} \tag{34}$$

the incoherent cross section can be expressed in the following form[1]:

$$
\begin{aligned}
\frac{d\sigma_{inc}}{d\Omega} &= \frac{d\sigma_p}{d\Omega}(q)(N(0, \sigma) - \frac{|F_S(q)|^2}{A}) + c_p Q^2 \\
Q^2 &= \pi \sigma^2 \int \frac{\partial \rho(b, z_2)}{\partial b} \frac{\partial \rho(b, z_1)}{\partial b} \rho(b, z_3) \theta(z_2 - z_1) \theta(z_3 - z_2) \\
&\times \exp(-\frac{\sigma}{2} \int_{z_1}^{\infty} \rho(b, z\prime) dz\prime - \frac{\sigma}{2} \int_{z_2}^{\infty} \rho(b, z\prime) dz\prime) b db dz_1 dz_2 dz_3
\end{aligned} \tag{35}
$$

Here $F_S(q)$ is the nucleus strong form factor evaluated by the expression (26). Only in the case when absorption is absent ($\sigma = 0$) the factorization similar to the expression (31) takes place. In figure 43 we show our calculations of incoherent cross sections for carbon target done by expressions (31)–(33) (dotted line) and expression (35) with oscillator potential (17).

Conclusions

Using Glauber multiple scattering theory we studied electromagnetic and strong amplitudes for the η meson photoproduction off light nuclei (carbon and helium). These calculations include:

- the η meson final state interaction in the nucleus;

---

[1] The derivation and detailed discussion of the incoherent production at small angles will be given elsewhere

- effect of light nuclei;

- contributions from nuclear collective excitations.

- the photon shadowing effect.

We also obtained the expression for incoherent cross section, which took the η absorption in nuclei into account. This study provides a solid foundation to extract the η meson radiative decay width from Primakoff experiment data with a high precision.

10 Rates and Uncertainties

10.1 Production Rates

In these experiments, the Primakoff amplitude will be extracted from the measured differential cross section for forward angle meson production. As mentioned earlier, the angular dependence will enable separation of the Primakoff amplitude from the background nuclear processes. We propose to perform a precision measurement of the differential cross sections on three targets, ^1H, ^4He, and ^{12}C over a range of angles $(0 - 4°)$ as determined by the electromagnetic calorimeter. The $1.18 \times 1.18 m^2$ calorimeter placed at a distance of $\sim 6.5 m$ from a $30 cm$ long liquid helium or hydrogen target and $1 cm$ thick ^{12}C target will provide a high geometrical acceptance for the two decay photons, yielding detection efficiencies of $\sim 60\%$. The expected experimental angular distribution from a Monte Carlo simulation of $\eta \rightarrow \gamma\gamma$ events for a 34 day run is shown in figure 44. In this simulation, the experimental resolutions and all efficiencies of the setup are taken into account.

In order estimate the production rate of $\eta \rightarrow \gamma\gamma$ events, we assume a 7×10^7 equivalent photons/sec incoherent bremsstrahlung photon beam on target. If one takes the upper 10% energy range of the tagged photon beam from 10.5 GeV to 11.7 GeV, the number of photons is $N_\gamma \sim 7.6 \times 10^6$ photons/sec. The integral of total coherent cross sections over the angular range of 0-3.5 degrees for these energies are: $\sim 1.1 \times 10^{-5}$ mb (10% for Primakoff) for proton targets, $\sim 1.6 \times 10^{-5}$ mb (21% for Primakoff) for ^4He, and $\sim 5.0 \times 10^{-5}$ mb (46% for Primakoff) for ^{12}C.

For a $30 cm$ long LH_2 target (3.46% r.l., $N(p) = 1.28 \times 10^{24}$ p/cm^2), the $\eta \rightarrow \gamma\gamma$ events rate is estimated as follows:

$$
\begin{aligned}
N(\text{exp. ev.}) \quad & = \quad \text{N(p)} \times \text{N(gamma)} \times (\text{Int. Cross Sec.}) \times (\text{eff.}) \times (\text{Br. Ratio}) \\
& = \quad 1.28 \times 10^{24} \times 7.6 \times 10^6 \times 1.1 \times 10^{-32} \times 0.6 \times 0.4 \\
& = \quad 2.57 \times 10^{-2} \text{ (events/sec)} \\
& \sim \quad 2220 \text{ (total } \eta \text{ events/day)} \\
& \sim \quad 222 \text{ (Primakoff events/day)}
\end{aligned}
$$

For a $30 cm$ long LHe^4 target (3.9% r.l., $N(^4He) = 5.64 \times 10^{23} He/cm^2$), the $\eta \rightarrow \gamma\gamma$ events rate is estimated as follows:

statistical	1.0%
photon flux	1.0%
target thickness	1.0%
acceptance, misalignment	0.5%
background substraction	0.7%
beam energy	0.2%
distorted form factor	0.6%
events selection	0.5%
branching ratio	0.66% (PDB)
Total	2.2%

Table 1: Estimation of the experimental uncertainties for $\Gamma(\eta \to \gamma\gamma)$ measurement.

$$
\begin{aligned}
\text{N(exp. ev.)} &= \text{N}(^4\text{He}) \times N(\gamma) \times \text{(Int. Cross Sec.)} \times \text{(eff.)} \times \text{(Br. Ratio)} \\
&= 5.64 \times 10^{23} \times 7.6 \times 10^6 \times 1.6 \times 10^{-32} \times 0.60 \times 0.4 \\
&= 1.65 \times 10^{-2} \text{ (events/sec)} \\
&\sim 1425 \text{ (total } \eta \text{ events/day)} \\
&\sim 300 \text{ (Primakoff events/day)}
\end{aligned}
$$

For a 5% r.l. ^{12}C target $(N(^{12}C) = 1.068 \times 10^{23} \text{ C/cm}^2)$, the $\eta \to \gamma\gamma$ events rate is estimated as follows:

$$
\begin{aligned}
\text{N(exp. ev.)} &= \text{N}(^{12}\text{C}) \times \text{N(gamma)} \times \text{(Int. Cross Sec.)} \times \text{(eff.)} \times \text{(Br. Ratio)} \\
&= 1.068 \times 10^{23} \times 7.6 \times 10^6 \times 5.0 \times 10^{-32} \times 0.6 \times 0.4 \\
&= 9.74 \times 10^{-3} (events/sec) \\
&\sim 840 \text{ (total } \eta \text{ events/day)} \\
&\sim 387 \text{ (Primakoff events/day)}
\end{aligned}
$$

10.2 Uncertainties

The estimated experimental uncertainties for $\Gamma(\eta \to \gamma\gamma)$ are listed in table 1. The total error for the $\eta \to \gamma\gamma$ decay width has been estimated to be on the level of 2.2%, which includes 1.0% statistical error and estimated systematic errors added in quadrature as shown in the table.

10.3 Beam Request

In order to accumulate a data sample with statistics of 1% for the integrated energy interval ($\sim$ 10,000 Primakoff events on each target), we request 45 days of beam time for the LH_2 target, 34 days for LHe^4 target, and 26 days of beam time for ^{12}C.

A summary of the requested beam time, specified for each major activity, is shown in the table below:

LH_2 target	45 days
LHe^4 target	34 days
^{12}C target	26 days
Empty target runs	5 days
Tagger efficiency, TAC runs	3 day
Setup, calibration, and checkout	7 days
Total	120 days

To reduce the uncertainties on the background subtraction, we plan to make runs with the same conditions as the physics runs but with the target removed from the beam line – the so called empty target runs. This will be done for each target. A total of 5 accumulated days will be required for these measurements. To control the photon flux in the experiment at the required 1% level, we will periodically measure the tagging efficency with the Total Absorption Counter. This will require a minimum configuration change, and we estimate total of 3 days for these measurements. Based on our experience from the first π^o run in Hall B, we request a total of 7 days for the experimental setup calibration and complete checkout with the beam. The major part of this time will be used for the HYCAL calorimeter precision calibration, optimization, and checkout of the trigger organization for the calorimeter. The calorimeter alignment should be within a $0.7mm$ accuracy in the plane perpendicular to the photon beam. Special measurements will be done for a better understanding of the HYCAL trigger efficiency. We estimate using one day of beam time for the trigger efficiency measurements.

In conclusion, we are requesting a total of 105 days of tagged photon beam time for the physics production data taking: 45 days for LH_2, 34 days for LHe^4, and 26 days for ^{12}C targets. In addition, we estimate 15 days for experimental setup, calibration, and empty target runs. Therefore, we request a total of 120 days of beam time for the precision measurement of the $\eta \to \gamma\gamma$ decay width with 1% statistical errors for each physics target.

11 Summary

We request 120 days of beam time to measure the $\Gamma(\eta \to \gamma\gamma)$ decay width at a precision of 2% level in Hall D. This experiment will not only resolve a long standing puzzle of the experimental discrepancy between the Primakoff and collider measurement results, but also significantly reduce the overall error bar on this important quantity (typical errors of the existing data listed in PDG [53] are from 7.6%–25.5%), which will result a direct improvement on all other partial η decay widths as well. Precise measurement of this quantity will have a significant impact on the experimental determination of fundamental parameters of QCD,

such as the ratio of light quark masses (m_u, m_d, m_s) and the $\eta - \eta'$ mixing angle and decay constants. At a more general level, this measurement provide important input to test chiral symmetry breaking, P, PC and C symmetries in QCD, and search for new physics beyond the standard model.

This is the first experiment in a series measurements planned in the *PrimEx* 12 GeV program. We believe the result of these future precision experiments will provide a new and powerful experimental window on QCD at JLab in an area where the basic theory has been reasonably well developed.

References

[1] Jefferson Lab PAC18 report, 2000.

[2] Jefferson Lab PAC23 report, 2003.

[3] M. Gell-Mann, R. J. Oakes, and B. Renner. Phys. Rev. 175 (1968) 2195.

[4] N.M.K. Nefkens and J.W. Price, Phys. Scr. **T99** (2002) 114.

[5] J.S. Bell and R. Jaciw, Nuovo Cimento 60A (1969) 47; S.L. Adler, Phys. Rev. 177 (1969) 2426.

[6] J. L. Goity, A. M. Bernstein and B. R. Holstein, Phys. Rev. D66 (2002) 076014.

[7] P. Herrera-Siklódy, J. I. Latorre, P. Pascual and J. Taron, Nucl. Phys. **B497** (1997) 345, and Phys. Lett. **B419** (1998) 326.

[8] R. Kaiser and H. Leutwyler, in Non-perturbative Methods in Quantum, Field Theory, A. Schreiber, A. G. Williams and A. W. Thomas, Editors, World Scientific (Singapore 1998), hep-ph/9806336. R. Kaiser and H. Leutwyler, Eur. Phys. J. **C17** (2000) 623.

[9] Th. Feldmann and P. Kroll, Eur. Phys. J. **C5** (1998) 327.
Th. Feldmann, P. Kroll and B. Stech, Phys. Rev. **D58** (1998) 114006.

[10] H. Leutwyler, Phys. Lett. B374 (1996) 181.

[11] Johan Bijnens and Jürg Gasser, Proceeding for the workshop on eta physics, Uppasala, October 25-27, 2001

[12] D. Haidt et al edit, Review of Particle Physics, Vol 3, (1998).

[13] A. Browman et al., Phys. Rev. Letts., vol. 33, no. 23, (1974)1400.

[14] N.A. Roe, Phys. Rev. **D50** (1994) 1451.

[15] A. Browman et. al., Phys. Rev. Lett. **33** (1974) 1400.

[16] G. Bellettini et al., Il Nuovo Cimento, vol. 66, no. 1, (1970), 243.

[17] T.E. Rodrigues, et. al., Phys. Rev. Lett. **101** (2008) 012301.

[18] J.M. Laget, Phys Rev. **C72** (2005) 022202.

[19] M. Branschweig, et al., DESY preprint, 70/1.

[20] "The Technical Design of the Hall-D Polarized Photon Beam at the Thomas Jefferson National Accelerator Facility", The GlueX Collaboration, Novermber 7, 2008.

[21] Jefferson Lab Hall D CDR, version 5.0.

[22] Silvia Niccolai, *Three-body photodisintegration of ^3He measured with CLAS*, Ph.D. thesis, George Washington University, 2003, unpublished.

[23] R. Bradford and R.A. Schumacher, CLAS-NOTE 2002-003, unpublished.

[24] R.A. Schumacher, CLAS-NOTE 99-010, unpublished.

[25] O. Klein and Y. Nishina, *Z. Phys.*, **52**, 853 (1929).

[26] I. Tamm, *Z. Phys.*, **62**, 545 (1930).

[27] I.M. Brown and R.P. Feynaman, *Phys. Rev.*, **85**, 231(1952).

[28] Till B. Anders, *Nucl. Phys.*, **87**, 721 (1967).

[29] K.J. Mork, *Phys. Rev.*, **A4**, 917 (1971).

[30] F. Mfandl and T.H.R. Skyrme, *Proc. R. Soc. London*, **A215**, 497 (1952).

[31] M. Ram and P.Y. Wang, *Phys. Rev. Lett.*, **26**, 476 (1971); *ibid.* **26**, 1210(E)(1971).

[32] A. H. Compton, Bull. Natl. Res. Counc. (U.S) 20, 19 (1922); *Phys. Rev.*, **21**, 483 (1923).

[33] Mykhailo Konchatnyi, PrimEx Note 37, http://www.jlab.org/primex/.

[34] A. Tkabladze, M. Konchatnyi, and Y. Prok, PrimEx Note 42, http://www.jlab.org/primex/.

[35] G. Morpurgo, Nuovo Cimento 31, 569 (1964)

[36] G. Fäldt, Nucl. Phys., B43, (1972) 591

[37] R. J. Glauber, High-energy physics and nuclear structure, Proc.of the 2nd Int. Conf., Rehovoth (1967)

[38] S. Gevorkyan, A. Gasparian, L. Gan, Primex Notes 45, 2007, URL: www.jlab.org/primex

[39] S. Gevorkyan, I. Larin, A. Gasparian, L. Gan, PrimEx Notes 46, 2007, URL: www.jlab.org/primex

[40] M. Abramowitz and I. Stegun, Handbook of Mathematical

[41] T. Bauer, R. Spital, D. Yennie, F. Pipkin, Rev. of Mod. Phys. 50, 261 (1978)

[42] L. Elton, Nuclear sizes (London,1962)

[43] C. Jager, H. Vries, C. Vries, Atomic Data and Nucl. Data Tables 14, 479 (1988)

[44] E. Offerman et al., Phys.Rev. C44, 1096 (1991)

[45] K. Gottfried, D. Yennie, Phys. Rev. 182, 1595 (1969)

[46] V. Glaser, R. Ferrell, Phys. Rev., 121, 886 (1961)

[47] R.J.Glauber, in: High-energy physics and nuclear structure, Proc.of the 2nd Int. Conf., Rehovoth (1967)

[48] W. Meyer et al. Phys. Rev. Lett. 28 (1972) 1344

[49] A. M. Boyarski et al. Phys. Rev. Lett. 23 (1969) 1343

[50] C. Engelbrecht, Phys. Rev. 133, B988 (1964)

[51] G. Bellettini et al., Nuovo Cim. LXVIA, N.1, 243 (1970)

[52] R. J. Glauber, G. Matthiae, Nucl.Phys. B21, 135 (1970)

[53] Phys. Lett. **B667** (2008) 590.
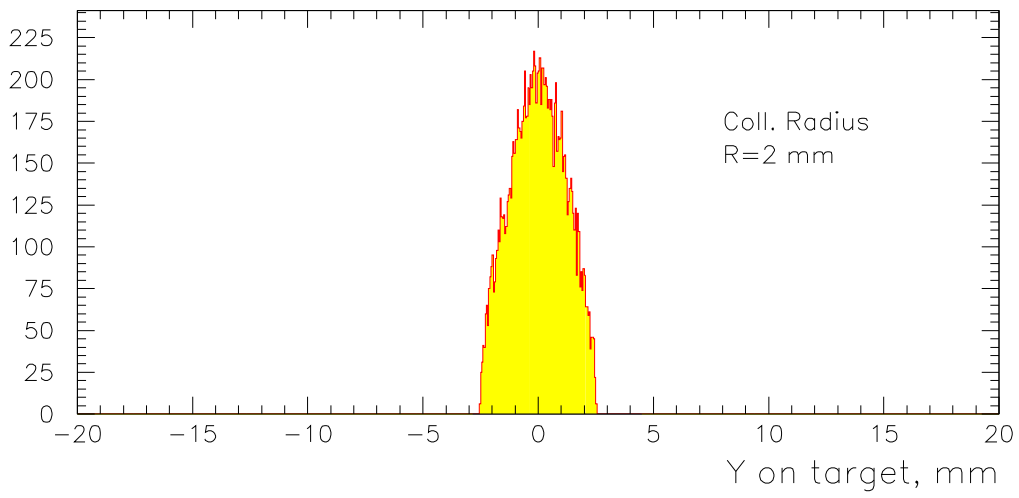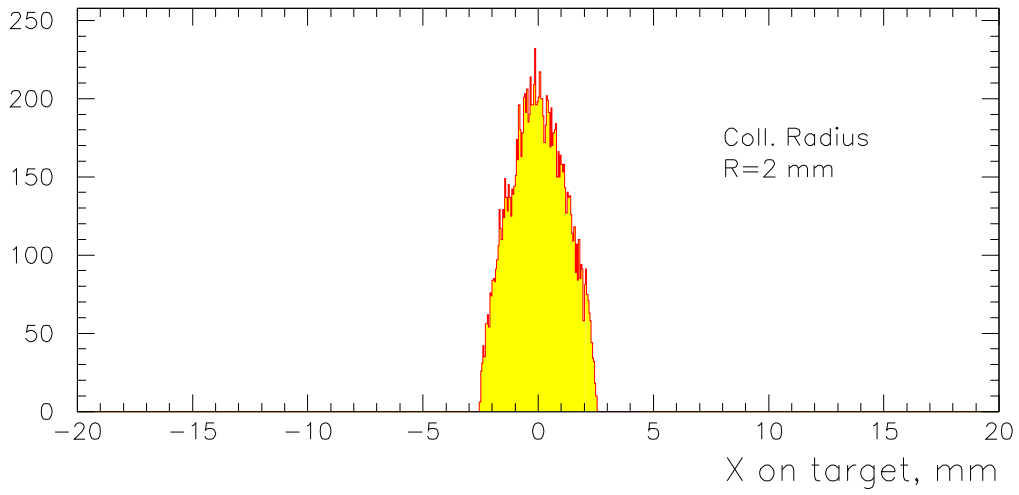
Figure 29: x and y distribution of the interaction vertex in the target for a collimator radius $R = 2mm$.
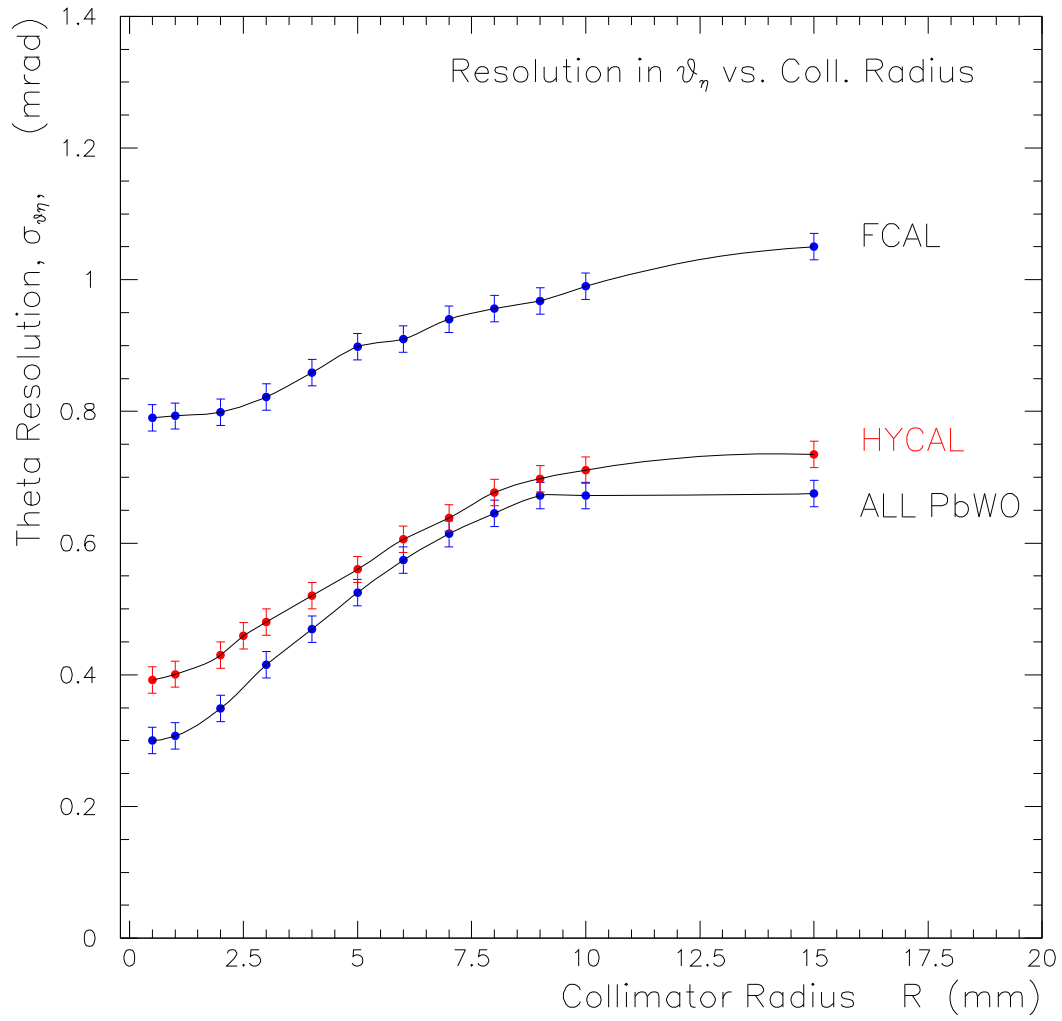
Figure 30: θ_η resolution *versus* collimator radius with the FCAL, HYCAL and upgraded HYCAL to all $PbWO_4$ crystal calorimeter.
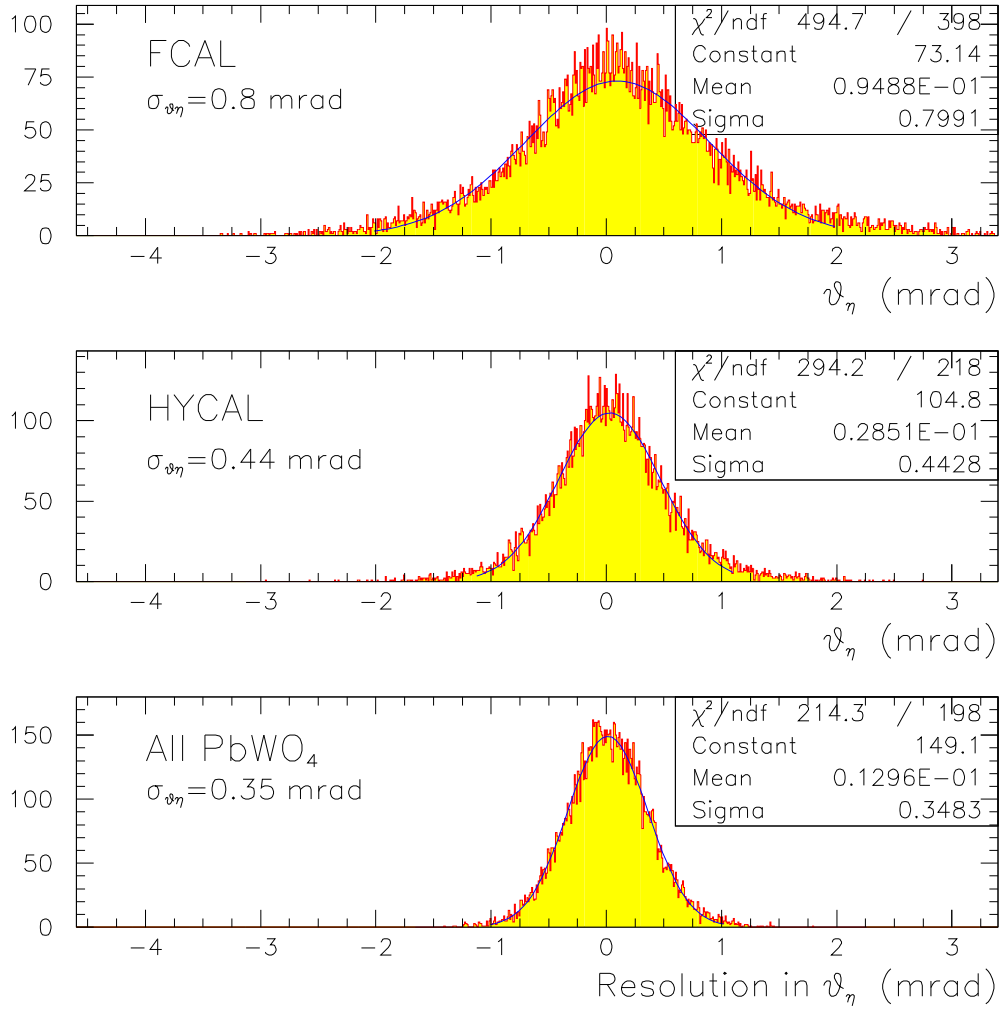
Figure 31: θ_η resolution for three different calorimeters: FCAL, HYCAL and upgraded HYCAL with all $PbWO_4$ crystal detectors.
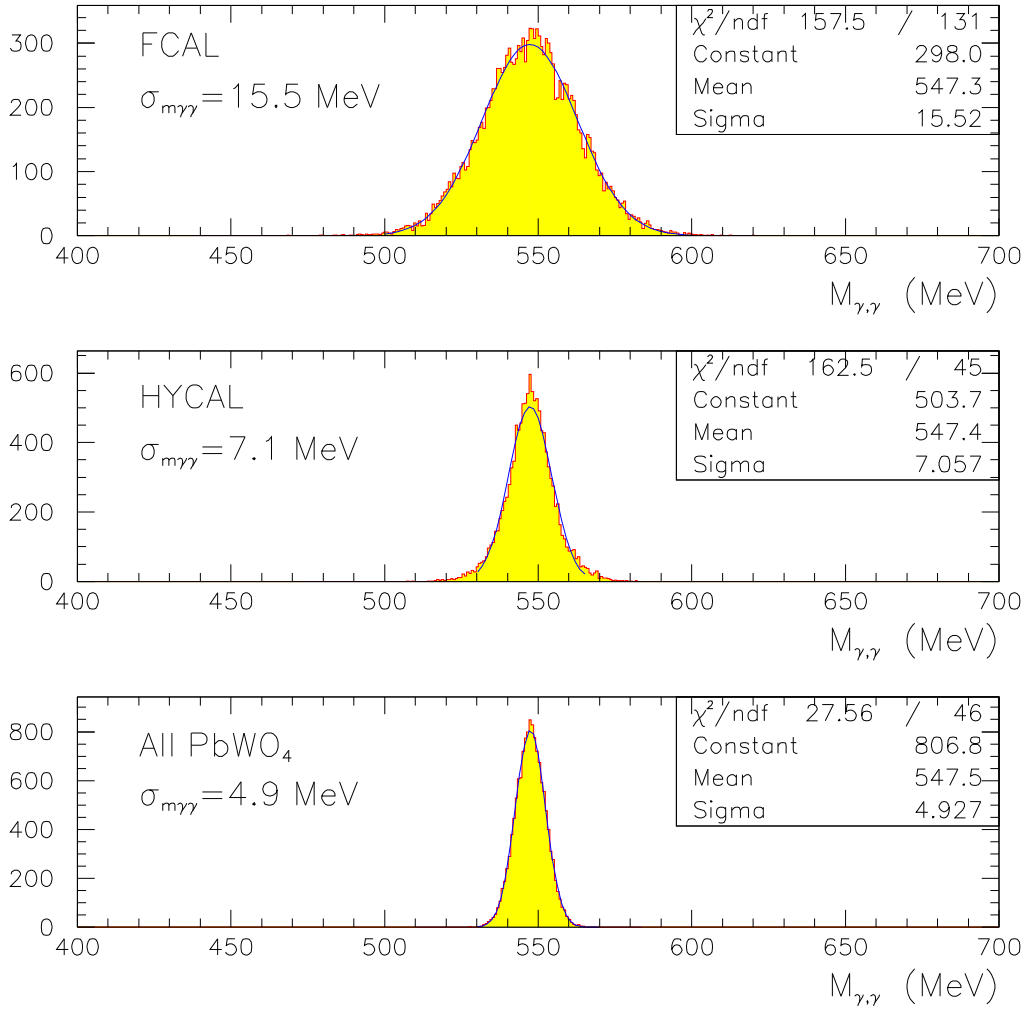
Figure 32: Invariant mass resolution for three different calorimeters: FCAL, HYCAL and upgraded HYCAL with all $PbWO_4$ crystal detectors.
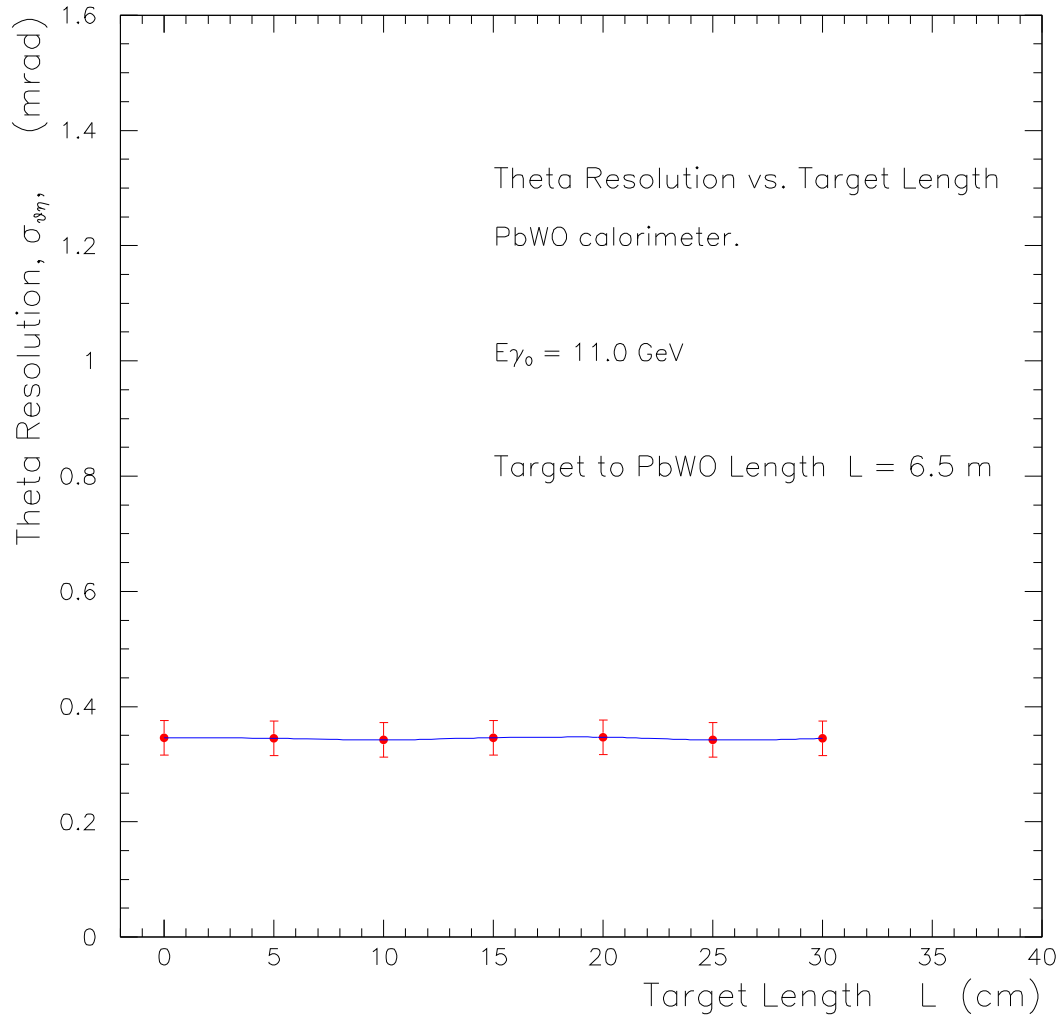
Figure 33: Expected resolutions in θ_η for different target lengths. The collimator radius is fixed at $R = 2mm$ for these simulations.
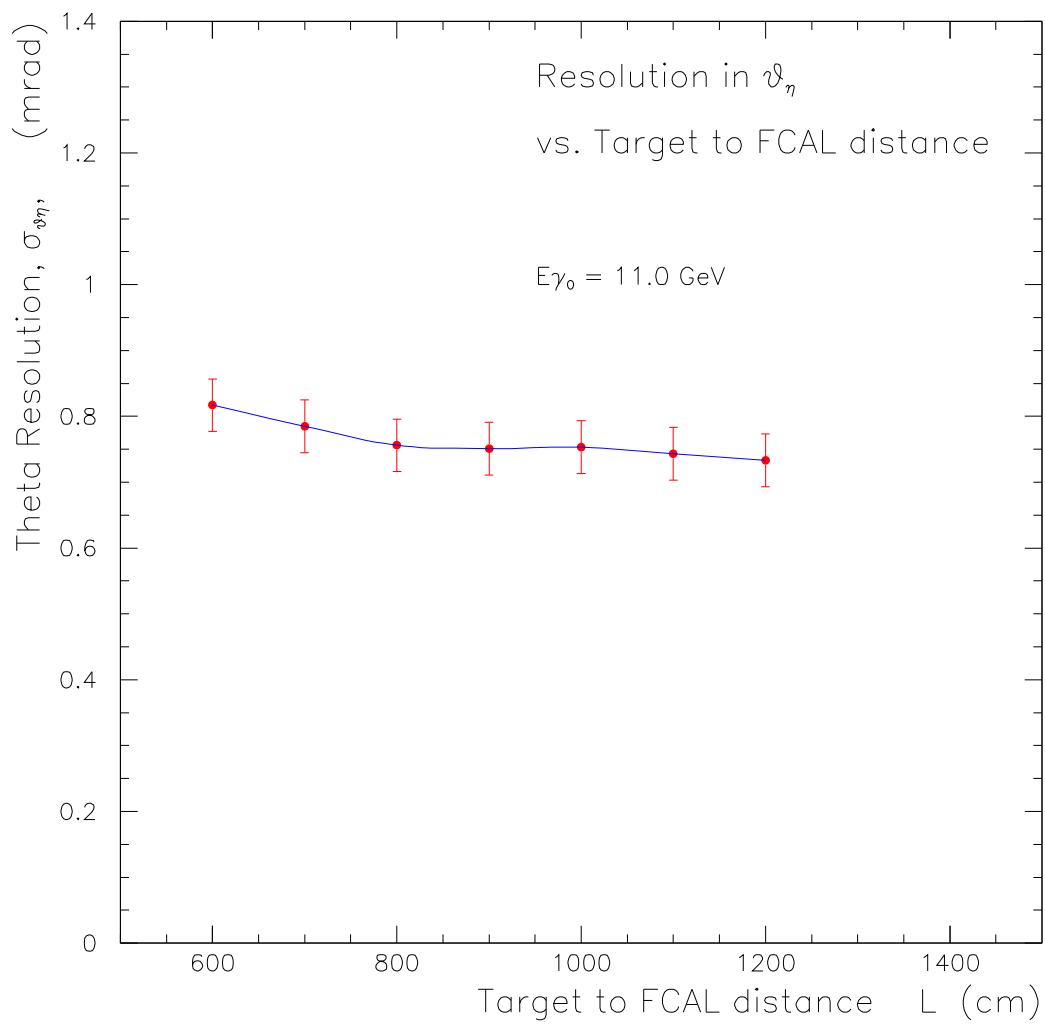
Figure 34: Expected θ_η resolutions *versus* target to FCAL distance.
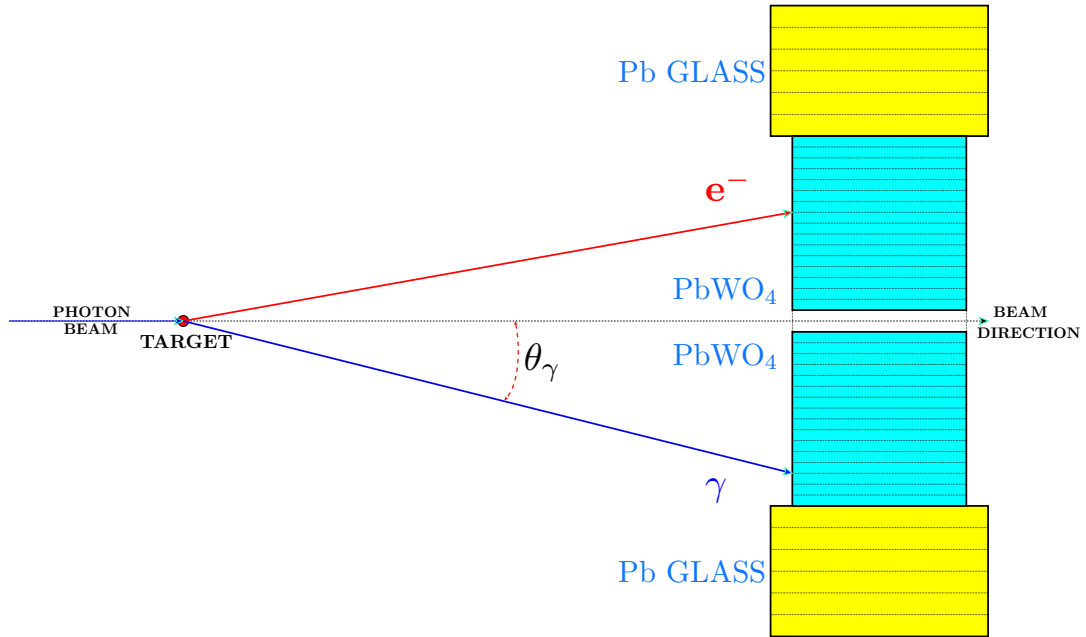
Figure 35: Detection of a single Compton event in HYCAL.
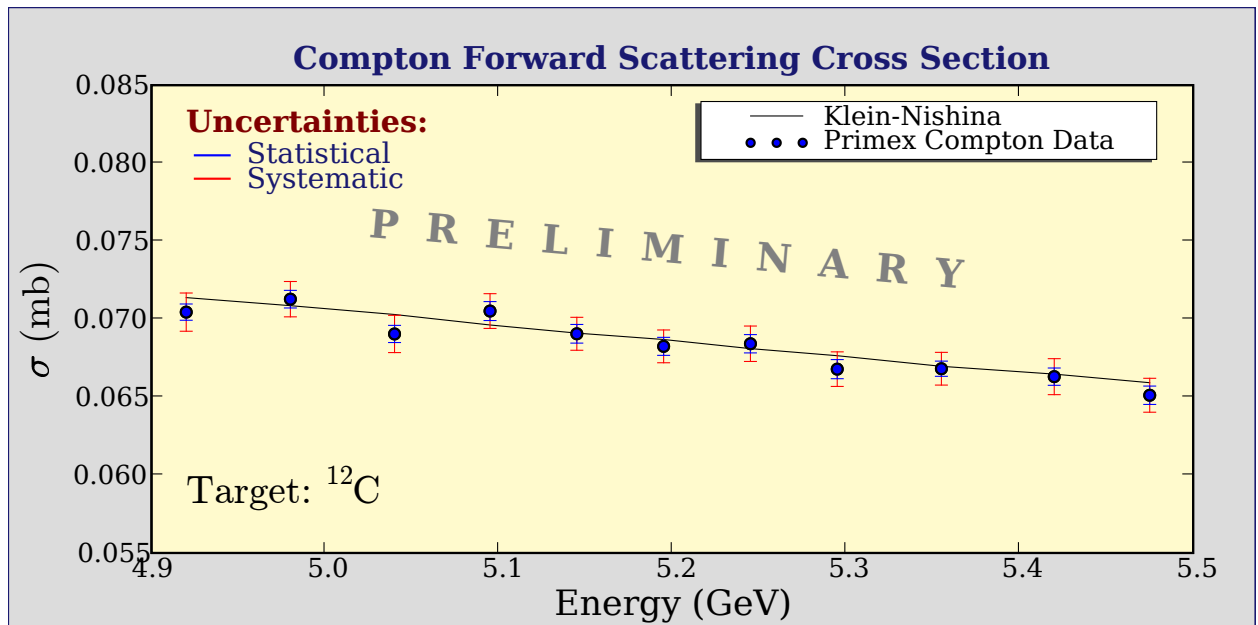
Figure 36: The forward Compton cross section averaged over the HYCAL acceptance. The statistical and systematic errors are shown in blue and red respectively. The data points are corrected with radiative corrections and double Compton scattering. The energy resolution for each point is about 1%.
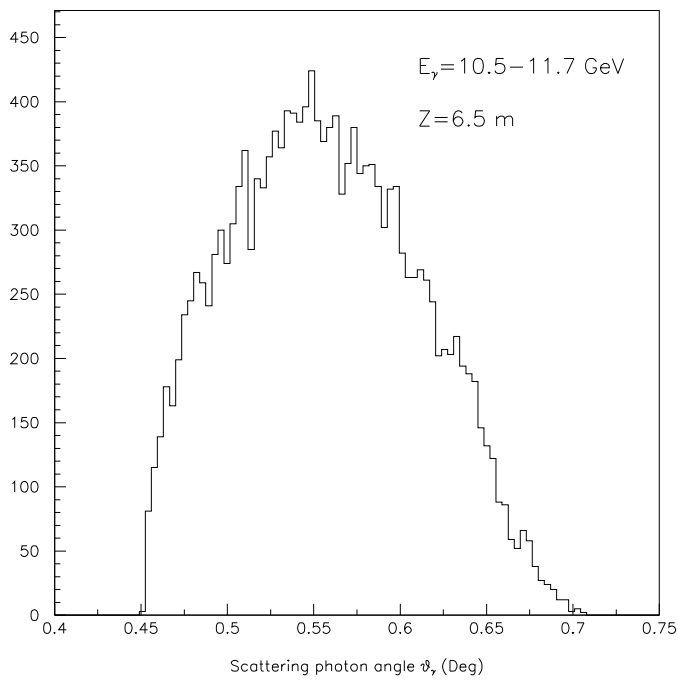
Figure 37: Monte Carlo results for Compton events detected over the HYCAL acceptance. A 10.25×10.25 cm^2 center hole in HYCAL is excluded in the acceptance and the distance between the target and HYCAL is $6.5m$.
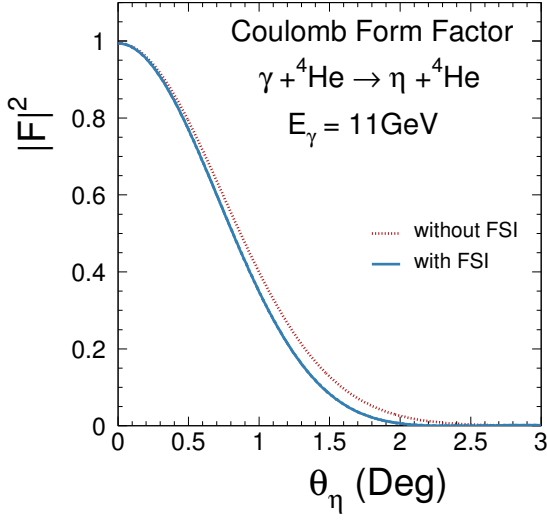
Figure 38: Coulomb form factor squared for ^{4}He. The solid line and the dashed line show with and without the final state interaction corrections.
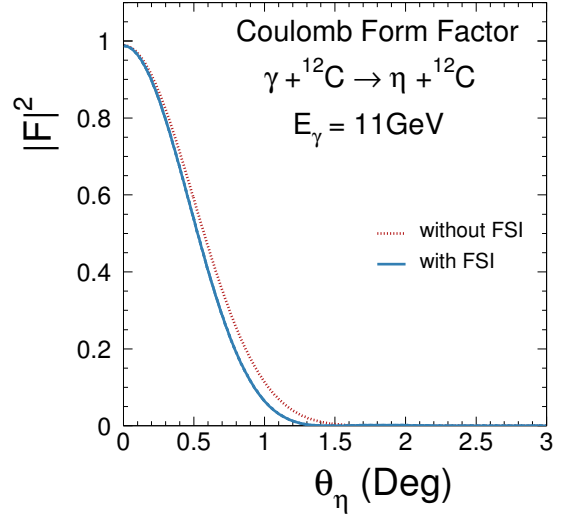
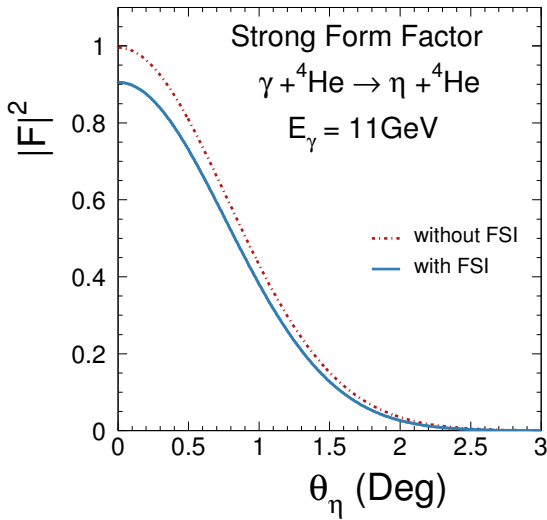Figure 39: Coulomb form factor squared for ^{12}C. The solid line and the dashed line show with and without the final state interaction corrections.

Figure 40: Strong form factor square for ^{4}He. The solid line and the dashed line show with and without the final state interaction corrections.
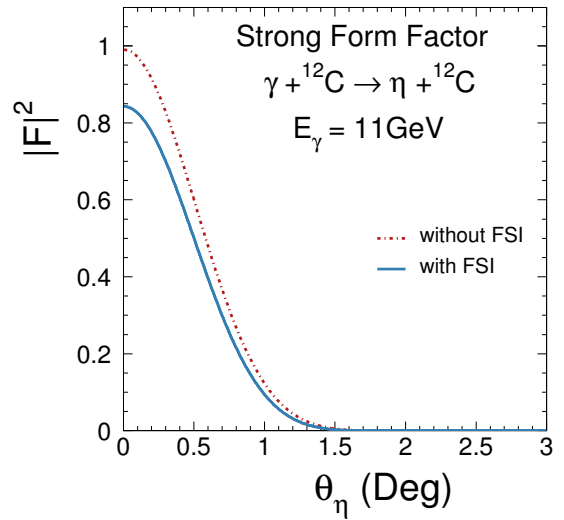

Figure 41: Strong form factor square for ^{12}C. The solid line and the dashed line show with and without the final state interaction corrections.
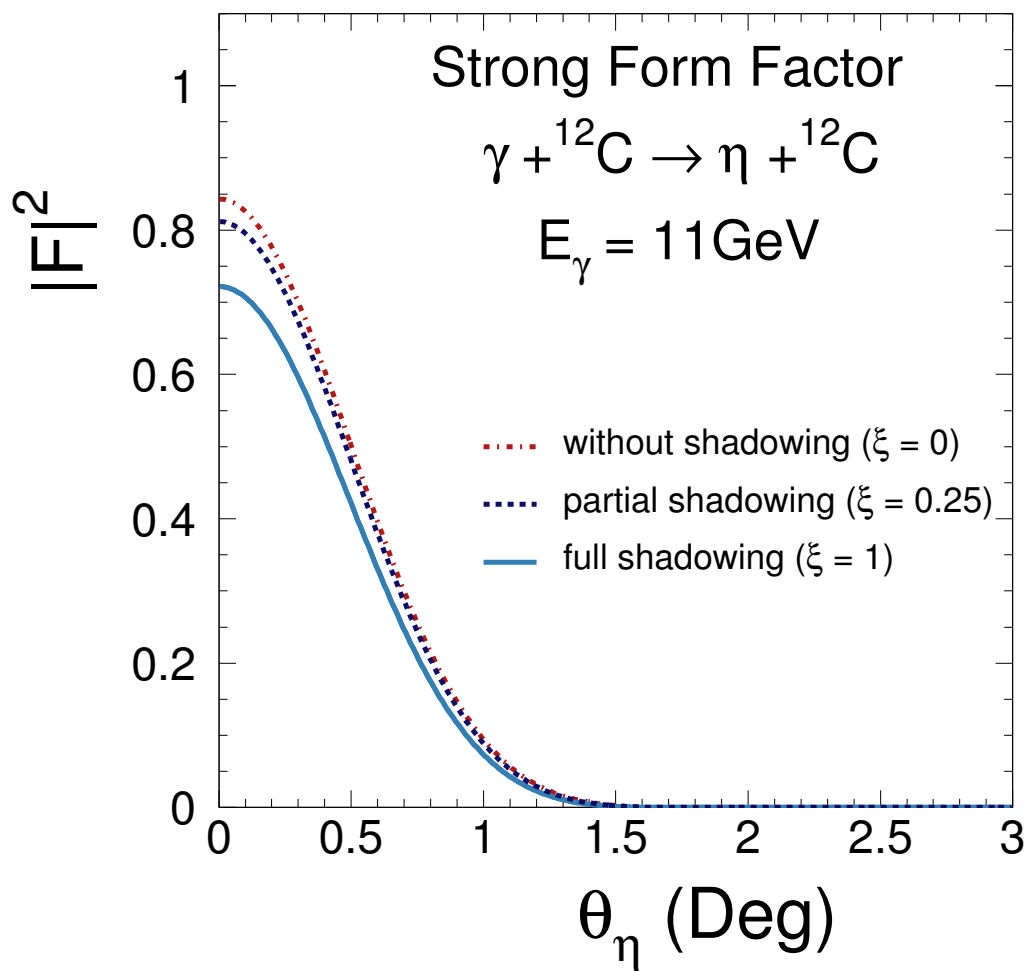
Figure 42: Strong form factor squared for ^{12}C calculated with different shadowing parameters.

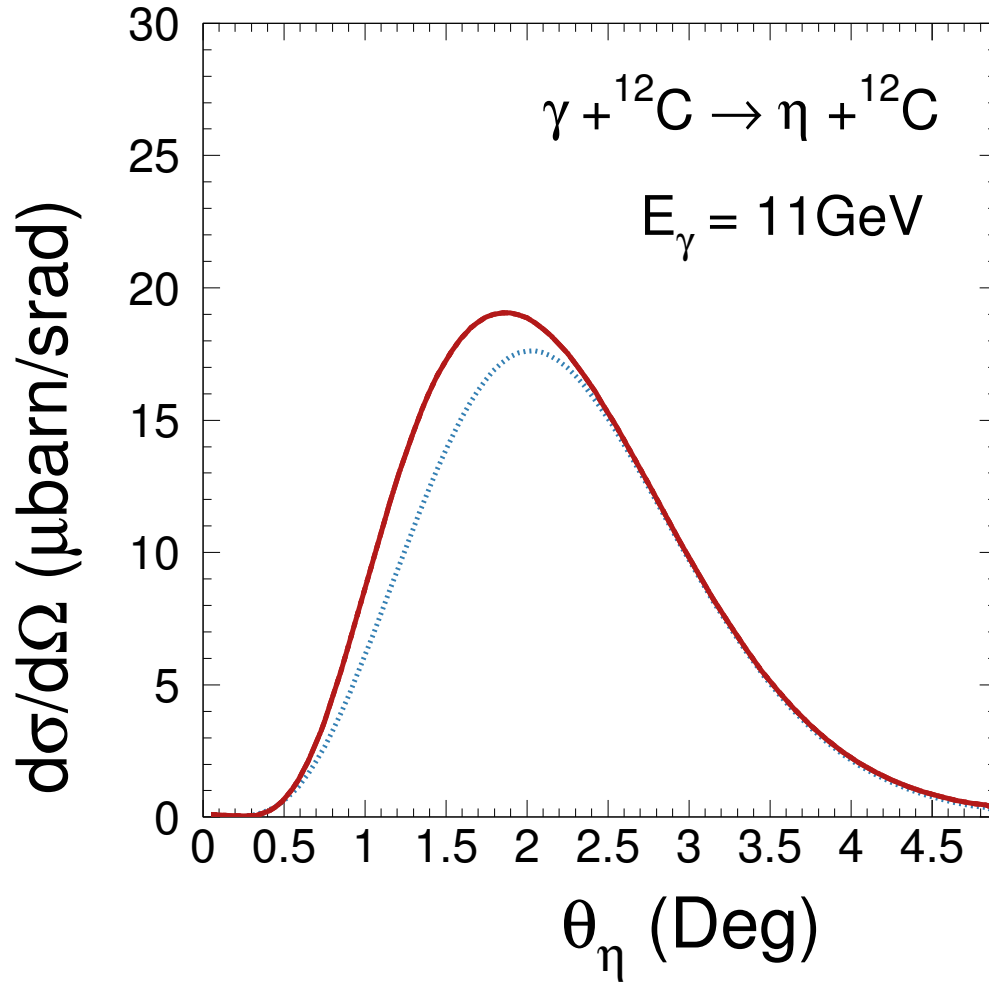Figure 43: Incoherent nuclear cross section for η photoproduction on ^{12}C. Dotted line is calculated by expressions (31)–(33) and solid line is calculated by expression (35) with oscillator potential (17).

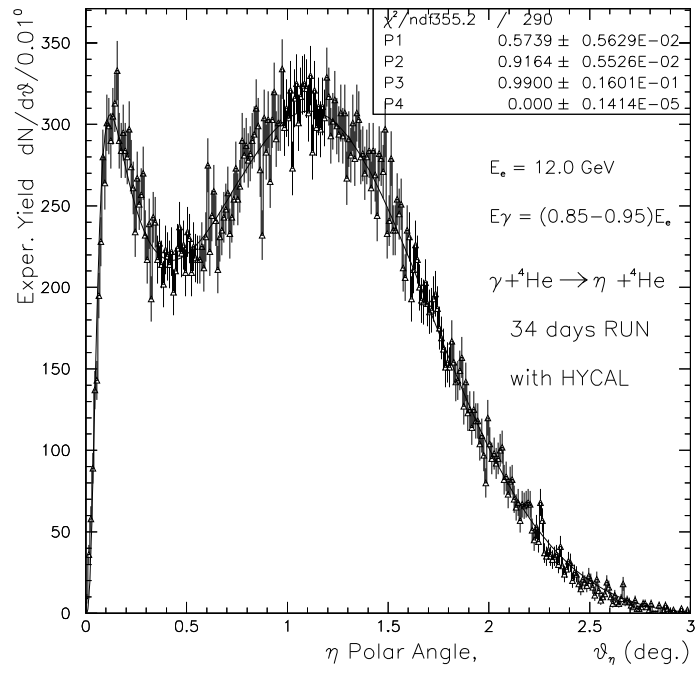Figure 44: Monte Carlo simulation of expected yield as a function of angle for $\eta \to \gamma\gamma$ events on ^4He.